nature medicine

ARTICLES

https://doi.org/10.1038/s41591-018-0085-8

A natural killer–dendritic cell axis defines checkpoint therapy–responsive tumor microenvironments

Kevin C. Barry[1,2], Joy Hsu[1,2], Miranda L. Broz[1,2], Francisco J. Cueto[1,3,4], Mikhail Binnewies[1], Alexis J. Combes[1,2], Amanda E. Nelson[1,2], Kimberly Loo[2,5,6], Raj Kumar[1,2], Michael D. Rosenblum[6], Michael D. Alvarado[6], Denise M. Wolf[7], Dusan Bogunovic[8], Nina Bhardwaj[9], Adil I. Daud[6], Patrick K. Ha[10], William R. Ryan[10], Joshua L. Pollack[11], Bushra Samad[1,2], Saurabh Asthana[2], Vincent Chan[1,2] and Matthew F. Krummel[1,2*]

Intratumoral stimulatory dendritic cells (SDCs) play an important role in stimulating cytotoxic T cells and driving immune responses against cancer. Understanding the mechanisms that regulate their abundance in the tumor microenvironment (TME) could unveil new therapeutic opportunities. We find that in human melanoma, SDC abundance is associated with intratumoral expression of the gene encoding the cytokine FLT3LG. FLT3LG is predominantly produced by lymphocytes, notably natural killer (NK) cells in mouse and human tumors. NK cells stably form conjugates with SDCs in the mouse TME, and genetic and cellular ablation of NK cells in mice demonstrates their importance in positively regulating SDC abundance in tumor through production of FLT3L. Although anti-PD-1 'checkpoint' immunotherapy for cancer largely targets T cells, we find that NK cell frequency correlates with protective SDCs in human cancers, with patient responsiveness to anti-PD-1 immunotherapy, and with increased overall survival. Our studies reveal that innate immune SDCs and NK cells cluster together as an excellent prognostic tool for T cell–directed immunotherapy and that these innate cells are necessary for enhanced T cell tumor responses, suggesting this axis as a target for new therapies.

Checkpoint blockade therapies, such as anti-CTLA-4 or anti–programmed cell death protein 1 (PD-1) immunotherapy, have been remarkably effective in reactivating T cell responses to tumors and providing long-lasting protection to patients. However, it is common for upwards of 80% of patients in any given indication to have no objective responses to these treatments[1]. Although the frequency of mutations leading to new T cell epitopes is suggested to be one factor associated with better responses[2], other immune parameters and cell types that control responsiveness to these treatments remain to be determined.

We previously identified a rare intratumoral dendritic cell (DC) subset that is uniquely capable of restimulating T cells in the TME[3] and is required for adoptive T cell therapy in mouse models[3–7]. These rare intratumoral type I conventional dendritic cells (cDC1; when taken from tumors, referred to as SDCs) were defined in mice by surface expression of the integrin CD103 and in humans by expression of thrombomodulin (BDCA-3; also known as CD141)[3]. Studies in lung have demonstrated that these cells are rarer in tumors than in adjacent normal tissues[8]. In the infrequent cases of WNT–β-catenin pathway mutations in melanoma, decreases in the number of these DCs have been implicated in poor outcome, and this has been mapped to defects in chemokine expression patterns in tumors[9]. Here we find that the relationship between SDC number and outcome is likely more generalized.

In this study, we show that the levels of protective BDCA-3$^+$ SDCs in the TME correlate with better overall survival (OS) of patients with melanoma. We further link the abundance of intratumoral SDCs to the expression of the gene encoding Fms-related tyrosine kinase 3 ligand (FLT3LG), the formative cytokine for cDC1. Using a novel *Flt3l* reporter mouse, we identify intratumoral lymphocytes as the producers of *Flt3l* in tumor, with genetic and functional studies demonstrating that natural killer (NK) cells are the integral cell type that produces *Flt3l* to control the levels of SDCs in tumor. We further show that SDCs in human melanoma correlate with levels of intratumoral NK cells and that both innate immune cell types correlate with responsiveness to anti-PD-1 immunotherapy. These findings suggest that NK cells, through the production of *FLT3LG* in tumor, control the levels of SDCs in tumor and increase the responsiveness of patients to anti-PD-1 immunotherapy.

Results

BDCA-3$^+$ SDC levels in human melanoma correlate with increased overall survival. Our previous work identified an eight-gene 'SDC signature', derived from direct comparisons of

[1]Department of Pathology, University of California San Francisco, San Francisco, CA, USA. [2]UCSF Immunoprofiler Initiative, University of California San Francisco, San Francisco, CA, USA. [3]Centro Nacional de Investigaciones Cardiovasculares Carlos III (CNIC), Madrid, Spain. [4]Department of Biochemistry, Faculty of Medicine, Universidad Autónoma de Madrid, Madrid, Spain. [5]Melanoma Clinical Research Unit, University of California San Francisco, San Francisco, CA, USA. [6]Department of Dermatology, University of California San Francisco, San Francisco, CA, USA. [7]Department of Laboratory Medicine, University of California San Francisco, San Francisco, CA, USA. [8]Department of Microbiology, Icahn School of Medicine at Mount Sinai, New York, NY, USA. [9]Tisch Cancer Institute, Icahn School of Medicine at Mount Sinai, New York, NY, USA. [10]Department of Otolaryngology, University of California San Francisco, San Francisco, CA, USA. [11]Pionyr Immunotherapeutics, San Francisco, CA, USA. *e-mail: matthew.krummel@ucsf.edu

SDCs versus all other myeloid populations within mouse tumors[3] (Fig. 1a). We used this SDC gene signature to estimate the number of SDCs across the spectrum of melanoma samples with associated clinical outcome data in a previously published metastatic melanoma dataset[10] and found that six 'SDC signature' genes had a significant individual association with increased OS from the time of metastasis (Supplementary Table 1). Furthermore, after binning the entire signature for each sample into 'high' or 'low' expression with a 66% stringency cutoff, we found that high expression significantly correlated with increased OS in Kaplan–Meier analysis (Fig. 1b); similar correlations were observed at 33% and 50% stringency (Supplementary Fig. 1a). The correlation of the SDC gene signature with increased OS was recapitulated in The Cancer Genome Atlas (TCGA) melanoma dataset (Supplementary Fig. 1b)[11]. We further found that measures of tumor-infiltrating lymphocyte (TIL) category were highly correlated with the SDC gene signature (Fig. 1c). Furthermore, expression of a gene signature that uses a ratio of signatures for SDCs and nonstimulatory myeloid cells (NSMs)[3], representing the relative abundance of stimulatory and inhibitory myeloid populations, also showed a strong correlation with OS and increased T cell infiltration (Supplementary Fig. 1c–e). These data suggest that the relative levels of SDCs in tumor correlate with increased OS.

Intratumoral SDC abundance predicts responsiveness to anti-PD-1 immunotherapy. Tumoral SDCs were first defined by their ability to cross-present tumor antigens to T cells and stimulate them[3,4] and have since been shown to be required for profound anti-PD-1 responses in mouse models[5–7]. We therefore sought to determine whether SDC levels related to the effectiveness of a T cell checkpoint blockade treatment, which would be predicted to release more $CD8^+$ T cells for possible tumor control[12]. To extend this analysis to patients with melanoma and to more broadly determine the immune components required for responsiveness to anti-PD-1 immunotherapy, we analyzed tumor biopsies from two independent cohorts (cohort A: $n=33$, all comers, including those already treated with various immunotherapies; cohort B: $n=23$, all pre-anti-PD-1 immunotherapy; Supplementary Table 2) of biopsies or surgical resections from patients with metastatic melanoma. Biopsies were digested into single-cell suspensions that were subsequently analyzed by flow cytometry and RNA sequencing (RNA-seq) while the clinical outcome of patients was tracked along with responsiveness to anti-PD-1 immunotherapy. Patients were parsed into groups either as 'nonresponders', defined as those with either stable or progressive disease, or 'responders', defined as those with partial or complete responses to anti-PD-1 therapy (see Methods). We designed a comprehensive flow panel to quantify the human immune infiltrates in tumor (Fig. 1d–f and Supplementary Fig. 2a,b), and although we found heterogeneity in the number of immune infiltrates across patients with melanoma, there was no significant correlation between total immune infiltrate and responsiveness to anti-PD-1 immunotherapy (Fig. 1d).

In contrast, multiple myeloid populations within the TME trended with response to immunotherapy (Fig. 1e,f). $CD14^-$ tumor associated macrophages (TAMs) showed a trend toward increased numbers in anti-PD-1 therapy–responding patients, but this was only seen in one cohort (Fig. 1e). High numbers of $CD14^+$ cells were negatively prognostic for responsiveness to anti-PD-1 immunotherapy in cohort B, whereas in cohort A, in which $CD14^+CD16^+$ monocytes could be effectively separated from $CD14^+CD16^-$ TAMs, increased intratumoral monocyte levels, more so than TAMs, trended with negative prognostic value for anti-PD-1 responsiveness (Fig. 1e). Further, BDCA-1^+ DCs (cDC2s) did not show a significant change that correlated with responder status in either cohort (Fig. 1f). Interestingly, a high proportion of BDCA-3^+ DCs (which were further confirmed to be cDC1 by staining for CLEC9a; Supplementary Fig. 2c) among total antigen-presenting cells (APCs; gating on $CD19^-$HLA-DR^+ cells) strongly predicted patient responsiveness to anti-PD-1 therapy in both melanoma cohorts (Fig. 1f).

***FLT3LG* expression correlates with SDC levels in tumor.** Given the profound association of SDCs with patient outcome and responsiveness to anti-PD-1 immunotherapy, we sought to determine the cellular and molecular mechanisms controlling the levels of protective myeloid cells in tumors. The formative cytokine for cDC1s, which include tumoral SDCs, is FLT3L[3,13], yet the endogenous source of this cytokine in cancer remains unknown. Using our melanoma dataset containing data from paired flow cytometry and RNA-seq of total live cells from tumor (cohort A; Supplementary Table 2), we found a significant correlation between the levels of

Fig. 1 | BDCA-3^+ DCs define overall outcome in melanoma patients and predict responsiveness to anti-PD-1 immunotherapy. a, Signature genes identifying SDCs (from ref. [3]). **b**, Kaplan–Meier plot for postrecurrence survival of patients with metastatic melanoma grouped by expression of genes in the SDC list. Data from ref. [10] ($n=44$ metastatic melanoma samples from 38 biologically independent patients) are parsed into 'high' ($n=15$ metastatic melanoma tumor samples) and 'low' ($n=29$ metastatic melanoma tumor samples) bins at a 66% stringency threshold for levels of expression of the SDC genes. The *P* value was calculated by log-rank test after adjusting for multiple comparisons using the Benjamini–Hochberg method. **c**, Class-based measures of TIL category from ref. [10] plotted versus the *z* score–normalized SDC gene signature ($n=33$ metastatic melanoma samples). For box-and-whisker plots: box ends, upper and lower quartiles; midline, median; error bars, maximum and minimum values. The regression line is superimposed. TIL categories are defined as: 0, 0–5% ($n=1$); 1, 5–25% ($n=13$); 2, 25–50% ($n=10$); 3, 50–100% ($n=9$). Correlation and two-tailed *P* value were assessed using the Pearson correlation coefficient and upaired *t*-test. **d**–**f**, Quantified frequency of $CD45^+$ immune cells among total live cells (**d**), macrophage and monocyte populations among HLA-DR^+ cells (**e**), and DC populations among HLA-DR^+ cells (**f**) in the tumors of patients. Patients are binned as either responders (Resp.; including partial or complete responses) or nonresponders (NonResp.; including stable disease and progressive disease). Data were collected from two independent patient cohorts, pooled across patients, and analyzed using the two-tailed unpaired parametric *t*-test. Data are presented as mean ± s.e.m., with all individual points shown. Cohort A: $n=26$ samples collected from 24 biologically independent patients (Resp.: $n=15$ samples from 15 patients, NonResp.: $n=11$ samples from 9 patients). Cohort B: $n=23$ biologically independent patient samples (Resp.: $n=9$ and NonResp.: $n=14$ independent patient samples). **g**, *z* score for *FLT3LG* expression in total live cells plotted versus the frequency of BDCA-3^+ DCs among total HLA-DR^+ cells in a subset of patients with melanoma in cohort A ($n=11$ biologically independent metastatic melanoma samples). Each point represents data from one patient, with the regression line superimposed (dotted red line); correlation and two-tailed *P* value were assessed using the Pearson correlation coefficient and upaired *t*-test. **h**, Percentile rank of SDC gene expression plotted versus normalized expression of *FLT3LG* in tumors from the TCGA melanoma dataset[11]. Correlation of $n=472$ independent patient samples was assessed using the Pearson correlation coefficient, and the two-tailed *P* value was calculated using an unpaired *t*-test. **i**, Kaplan–Meier plot for OS of patients with melanoma median split for *FLT3LG* gene expression. Data from ref. [11] are parsed into 'high' ($n=227$ biologically independent patient samples) and 'low' (red; $n=227$ biologically independent patient samples) *FLT3LG* expression bins at a 50% stringency threshold for levels of expression of *FLT3LG*. Plots and statistics were generated by the University of Zurich (UZH) TCGA Cancer Browser[28]. Shaded regions identify the 95% confidence interval, and the *P* value was calculated by log-rank test.

BDCA-3$^+$ DCs and expression of *FLT3LG* within tumor (Fig. 1g). We confirmed this correlation between SDC levels in tumor and the expression of *FLT3LG* using the SDC gene signature to estimate SDC levels in the public TCGA melanoma dataset[11] (Fig. 1h). TCGA melanoma samples[11] with high *FLT3LG* expression (median split) had significantly increased OS (Fig. 1i), consistent with an important role for FLT3LG in controlling SDCs in tumor. These findings suggest that control of the cytokine FLT3LG in the TME can have an important effect on the levels of SDCs, a cell type integrally important for immune responses to cancer and responsiveness to anti-PD-1 immunotherapy.

Lymphocytes are the primary producer of FLT3L in the tumor microenvironment. The correlation of *FLT3LG* expression and SDC levels in tumor introduced the question of which cell type(s) produce FLT3L. We therefore generated a *Flt3l*-reporter mouse by introducing DNA encoding an inducible Cre and teal fluorescent protein (TFP) downstream of the endogenous mouse *Flt3l* locus (Fig. 2a). Mice bearing ectopic B16F10 tumors that are homozygous for this allele have similar proportions of conventional DCs and lymphocytes within the TME despite a small but reproducible decrease in total serum FLT3L, suggesting that the protein remains functional to a similar extent within tumors (Supplementary Fig. 3a–c).

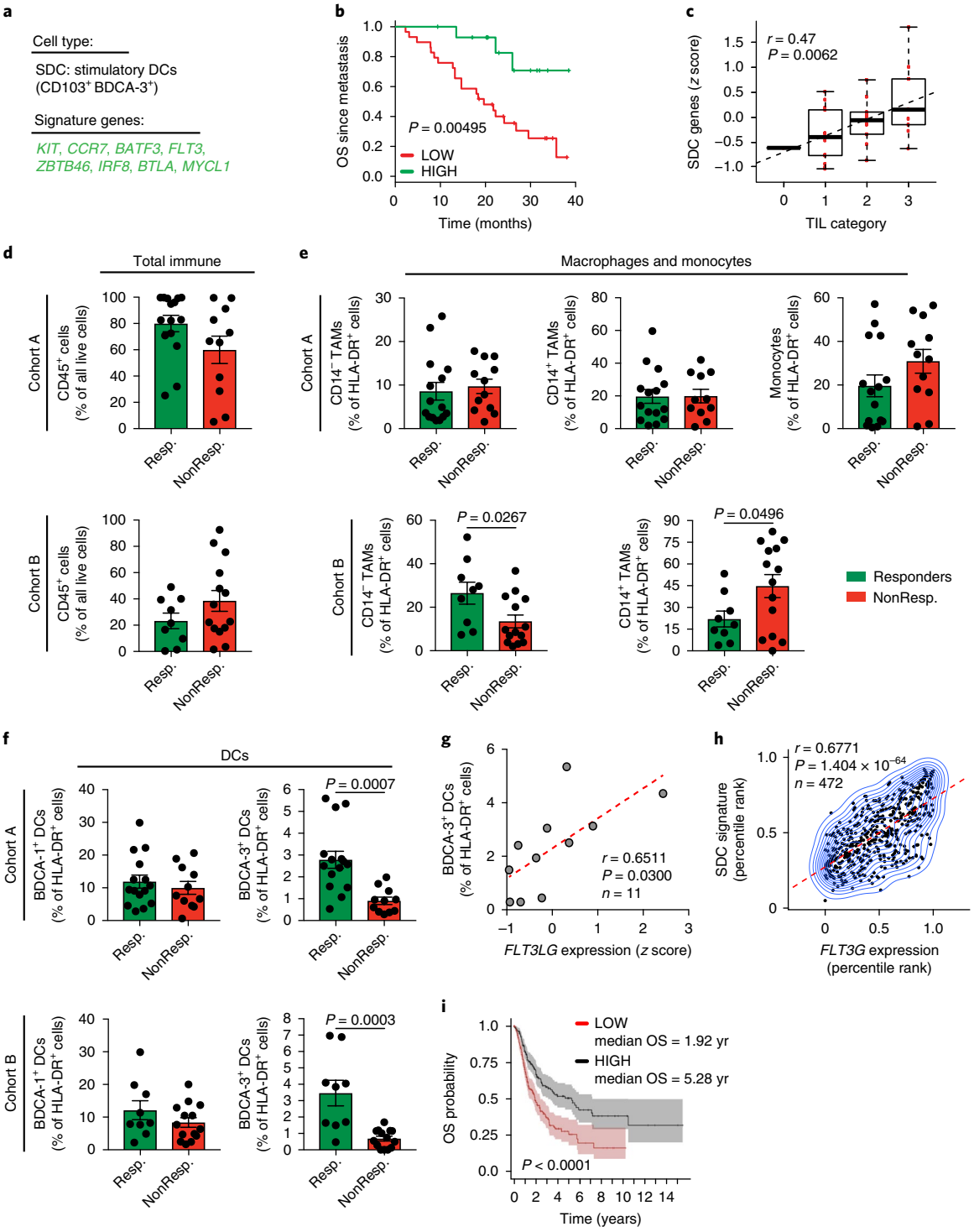

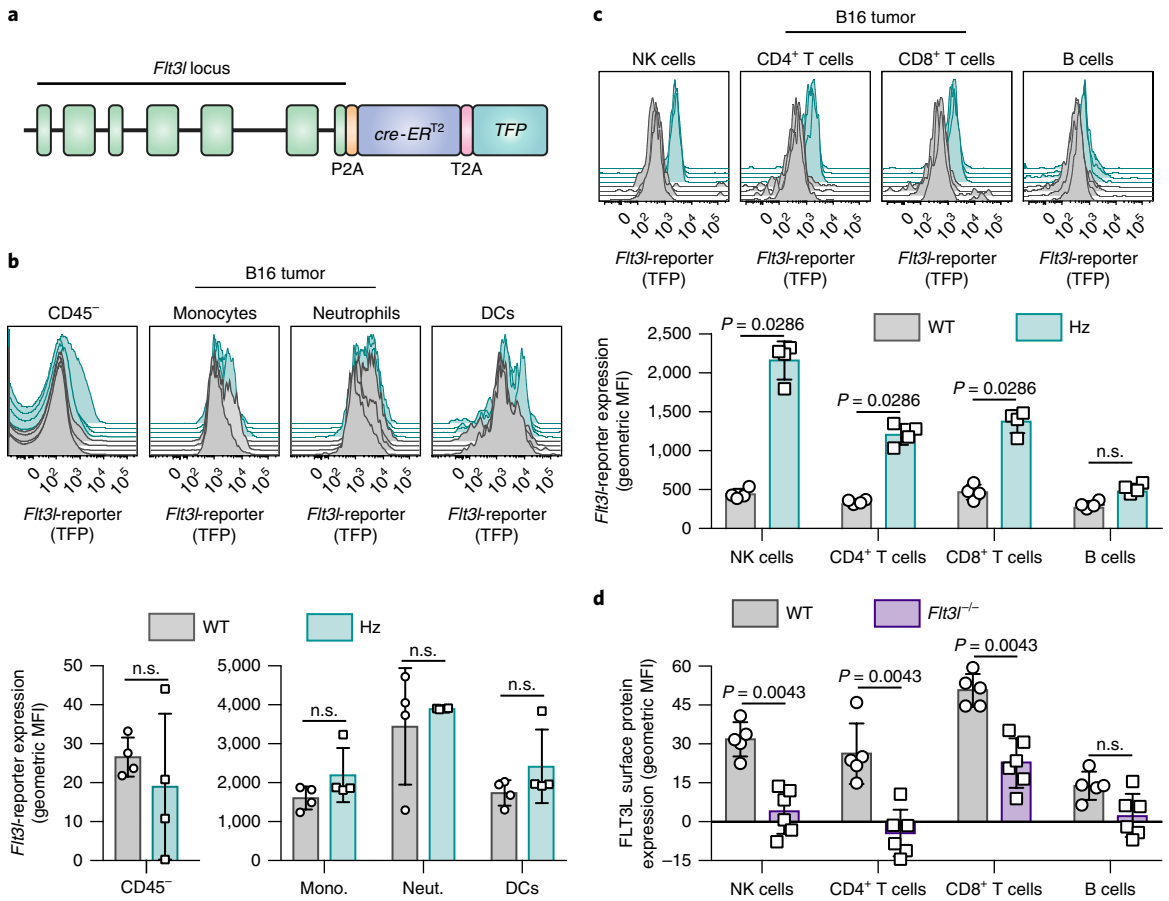

Fig. 2 | Tumor-resident lymphocytes produce FLT3L. a, Diagram of the *Flt3l* locus in the *Flt3l*-reporter mouse. *cre-ER*^{T2} encodes a tamoxifen-inducible Cre-recombinase. P2A, porcine teschovirus-1 2A self-cleaving peptide; T2A, thosea asigna virus 2A self-cleaving peptide. **b**, Representative flow plots (top) and geometric mean fluorescent intensity (MFI) (bottom) of *Flt3l*-reporter expression in CD45$^-$ and myeloid cells found in 2-week-old B16F10 tumors in WT ($n = 4$ biologically independent animals) and *Flt3l*-reporter homozygous (HZ; $n = 4$ biologically independent animals) mice. Monocytes, CD11b$^+$CD45$^+$Ly6C^{hi} cells; neutrophils, CD11b$^+$CD45$^+$Ly6C^{mid} cells; DCs, CD24$^+$CD45$^+$CD45R$^-$CD90.2$^-$Ly6G$^-$NK1.1$^-$Ly6C$^-$F4/80$^-$MHC-II$^+$ cells. **c**, Representative flow plots and geometric MFI of *Flt3l*-reporter expression in NK cells, CD4$^+$ T cells, CD8$^+$ T cells, and B cells (MHC-II$^+$B220$^+$) in 2-week-old B16F10 tumors in WT ($n = 4$ biologically independent animals) and *Flt3l*-reporter homozygous ($n = 4$ biologically independent animals) mice. For **b** and **c**, the gating strategy is depicted in Supplementary Fig. 3. **d**, Geometric MFI for FLT3L surface protein on NK cells, CD4$^+$ T cells, CD8$^+$ T cells, and B cells found in 2-week-old B16F10 tumors in WT ($n = 5$ biologically independent animals) or *Flt3l*-deficient ($n = 6$ biologically independent animals) mice stained with anti-FLT3L antibody. In all panels, data are plotted as mean ± s.d. Data were analyzed using the Mann–Whitney U Test to generate two-tailed *P* values. n.s., not significant. Data are representative of three (**b**,**c**) and two (**d**) independent replicates.

Flt3l-reporter homozygous mice were injected with ectopic B16F10 tumors, and at 2 weeks following tumor transplant, TFP, as a readout of *Flt3l* expression, was only detected within lymphocytes (Fig. 2b,c). Of the lymphocytes expressing *Flt3l*, NK cells had the highest expression levels, with lower levels in T cells and no significant expression in B cells (Fig. 2b,c; gating strategy in Supplementary Fig. 3e,f). These same populations were positive when stained with an anti-FLT3L antibody to detect the protein on cell surfaces (Fig. 2d). *Flt3l*, measured by TFP expression, was expressed at similar levels in NK cells isolated from tumor, tumor-draining lymph node (LN), and non-tumor-draining LN (Supplementary Fig. 3d), suggesting that *Flt3l* expression is not modulated by the TME. Similar patterns of expression for the reporter allele were found in other tumor models, including those that arise spontaneously (for example, the polyoma middle T antigen breast cancer model, engineered to express mCherry and ovalbumin (PyMTChOVA)[14]; Supplementary Fig. 4a,b). Interestingly, wild-type (WT) B16F10 tumor-bearing animals have no significant differences in FLT3L levels in serum, suggesting that local production of FLT3L is important for SDC levels and protection from cancer (Supplementary Fig. 4c).

FLT3L production by lymphocytes is required for normal SDC levels in tumor. We next undertook genetic experiments in mice to test the requirement for lymphocytes and their subsets in controlling the levels of SDCs in the TME. *Il2rg*$^{-/-}$ mice, which lack T cells and NK cells (Supplementary Fig. 5a), were injected with ectopic B16F10 melanoma, and tumors were analyzed for the levels of myeloid and lymphoid cells. Although B16F10 tumors from *Il2rg*$^{-/-}$ mice had roughly the same tumor area as their WT controls, tumors from *Il2rg*$^{-/-}$ animals had significantly reduced frequencies of CD103$^+$ SDCs in the TME, with no significant change in CD11b$^+$ DCs (Fig. 3a and Supplementary Fig. 5a). To test the role of FLT3L production specifically by lymphocytes in controlling the levels of SDCs, we generated mixed bone marrow chimeras with *Il2rg*$^{-/-}$ bone marrow mixed with either WT or *Flt3l*$^{-/-}$ bone marrow transferred into lethally irradiated *Flt3l*$^{-/-}$ recipient animals (Fig. 3b). *Il2rg*$^{-/-}$:*Flt3l*$^{-/-}$ mixed bone marrow chimeras, which have a lymphocyte compartment unable to produce FLT3L, had reduced levels of CD103$^+$ SDCs in tumor as compared to WT mice or *Il2rg*$^{-/-}$:WT mixed bone marrow chimeras, which had a lymphocyte compartment capable of producing FLT3L (Fig. 3b). The differences in CD103$^+$ SDC levels

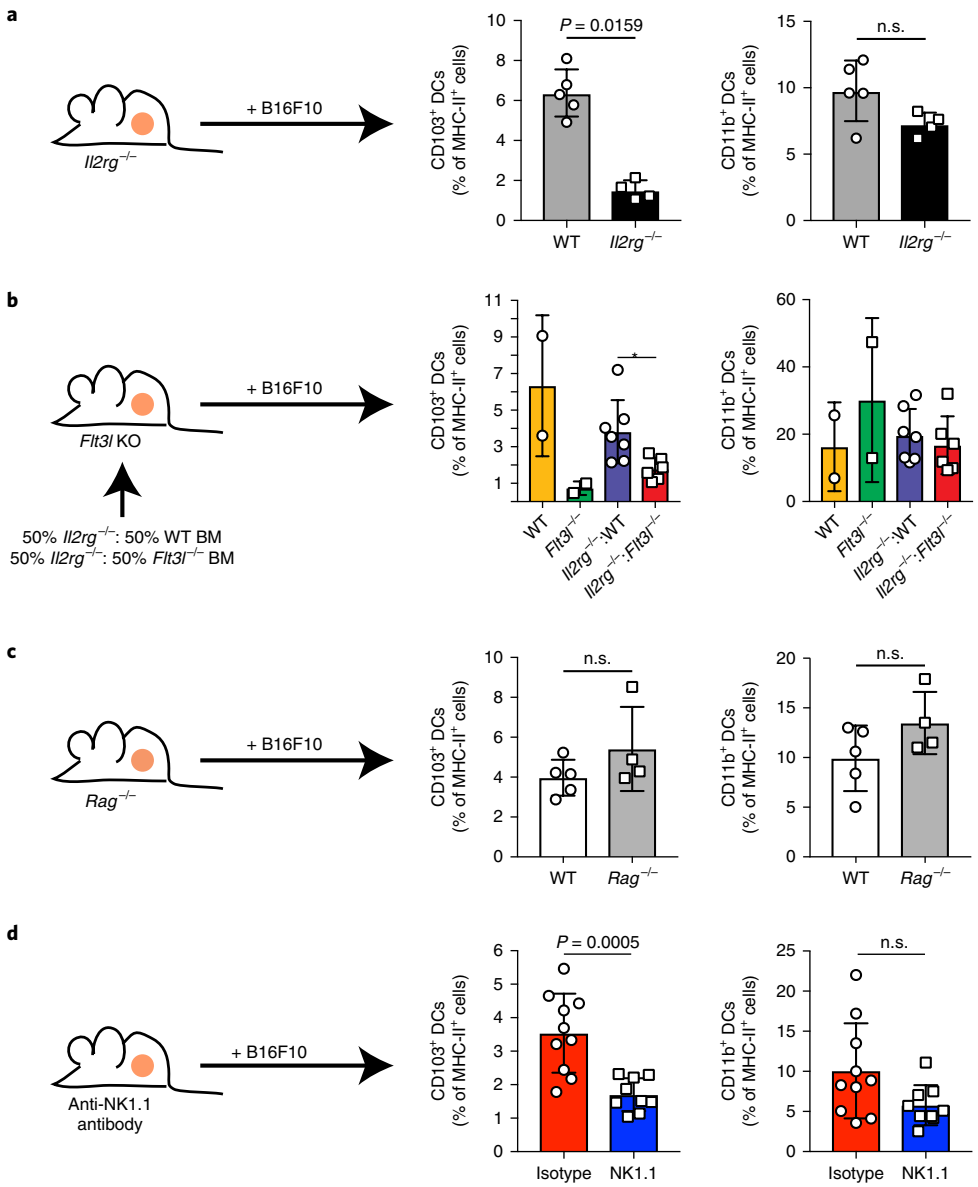

Fig. 3 | FLT3L production by NK cells controls the levels of CD103⁺ SDCs in tumor. a, The frequencies of CD103⁺ and CD11b⁺ DCs among total MHC-II⁺ cells in 2-week-old ectopic B16F10 tumors from WT ($n=5$ biologically independent animals) or *Il2rg*$^{-/-}$ ($n=4$ biologically independent animals) mice. **b**, The frequencies of CD103⁺ and CD11b⁺ DCs among total MHC-II⁺ cells in 2-week-old ectopic B16F10 tumors from mixed bone marrow chimeras, which were reconstituted with a 50:50 mixture of *Il2rg*$^{-/-}$:WT ($n=7$ biologically independent animals) or *Il2rg*$^{-/-}$:*Flt3l*$^{-/-}$ ($n=6$ biologically independent animals), and from WT ($n=2$ biologically independent animals) and *Flt3l*$^{-/-}$ ($n=2$ biologically independent animals) controls. *$P=0.0140$. Data are combined from two independent experimental replicates. **c**, The frequencies of CD103⁺ and CD11b⁺ DCs among total MHC-II⁺ cells in 2-week-old B16F10 tumors from WT ($n=5$ biologically independent animals) or *Rag*$^{-/-}$ ($n=4$ biologically independent animals) mice. **d**, The frequencies of CD103⁺ and CD11b⁺ DCs among total MHC-II⁺ cells in 2-week-old B16F10 tumors from WT mice treated with isotype control ($n=10$ biologically independent animals) or anti-NK1.1 antibody ($n=9$ biologically independent animals) every 3 d starting 3 d before tumor injection. In all panels, data are plotted as mean ± s.d. Data were analyzed using the Mann–Whitney U Test (**a**–**c**) or unpaired parametric *t*-test (**d**) to generate two-tailed *P* values. In all panels, data are representative of two independent experimental replicates.

in tumor are not due a global loss of T or NK cells, as these cells were, if anything, more abundant in tumor draining and nondraining LN of *Il2rg*$^{-/-}$:*Flt3l*$^{-/-}$ bone marrow chimeras (Supplementary Fig. 5b). CD11b⁺ DCs in tumors of *Il2rg*$^{-/-}$:*Flt3l*$^{-/-}$ mixed bone marrow chimeras were not significantly reduced as compared to *Il2rg*$^{-/-}$:WT bone marrow chimeras (Fig. 3b); furthermore, in tumor draining and nondraining skin LN, there was no defect in resident or migratory CD11b⁺ DCs, suggesting there is not a global defect in the CD11b⁺ DC compartment in the *Il2rg*$^{-/-}$:*Flt3l*$^{-/-}$ mixed bone marrow chimeras (Supplementary Fig. 5c). Interestingly, the levels of resident CD8⁺ DCs and migratory CD103⁺ DCs in tumor draining and nondraining LN were also reduced in the *Il2rg*$^{-/-}$:*Flt3l*$^{-/-}$ bone marrow chimeras, suggesting that the lymphocyte requirement extends to cDC1 production more generally (Supplementary Fig. 5c).

NK cells, not T cells, control SDC abundance in the tumor. To directly test the role of specific types of lymphocytes in controlling CD103⁺ SDC levels in tumor, we depleted T cells and NK cells, both of which express the *Flt3l*-reporter, in the mouse B16F10 melanoma model. Mice lacking all T cells as a consequence of a recombination

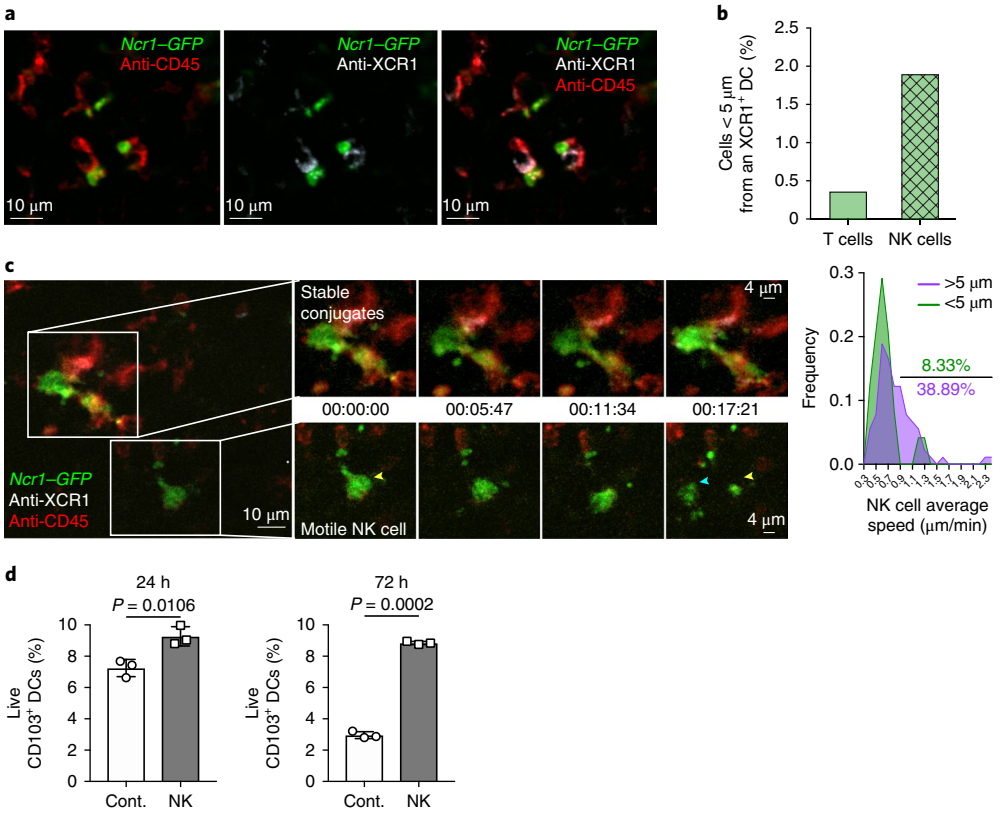

Fig. 4 | NK cells make frequent, stable interactions with XCR1⁺ DCs and provide prosurvival signals. a, Still images from live two-photon imaging of ectopic B78 melanoma tumor slices from mice expressing *Ncr1-GFP* (green) that were stained with anti-XCR1 (white) and anti-CD45 (red) antibodies to show static interactions between NK cells and XCR1⁺ DCs. Representative images from three biologically independent tumors are shown; also see Supplementary Video 1. **b**, Quantification of the number of transferred *actin-CFP*-expressing OT-I CD8⁺ T cells and endogenous NK cells less than 5 μm from a XCR1⁺ DC in B78-cherryOVA tumors in a triple-reporter mouse expressing *Ncr1-GFP*, *Xcr1-Venus*, and *Cd11c-mCherry*. The graph depicts the percentage of total imaged OT-I T cells and NK cells less than 5 μm from a XCR1⁺ DC. Still images from two biologically independent tumors were used for calculations. **c**, Left, Still images of dynamic NK cell–DC interactions. Insets show a time series of two regions of interest: where NK cells are in close proximity (< 5 μm) to XCR1⁺ DCs and are making stable interactions (top) and where a NK cell is greater than 5 μm from a XCR1⁺ DC with much more motility (bottom). Yellow arrow head, NK cell starting point. Blue arrow head, NK cell ending point. Images are representative of three independent biological replicates; also see Supplementary Video 2. Right, Quantification of speed of NK cells ($n = 114$ individual cells) parsed according to proximity to XCR1⁺ DCs (< 5 μm or > 5 μm from an XCR1⁺ DC). Speeds were binned into 22 bins ranging from 0.3 to 2.4 μm/min. **d**, Survival of CD103⁺ DCs from pooled steady-state mouse LNs that were sorted and incubated with WT NK cells, as measured by staining with viability dye at 24 h and 72 h of incubation ($n = 3$ technical replicates per treatment group). Cont., media-only control. Data are representative of three biological replicates.

activating gene (*Rag*) mutation had no defect in CD103⁺ DC levels in tumor (Fig. 3c and Supplementary Fig. 5d). Additionally, WT mice depleted of CD4⁺ or CD8⁺ T cells through use of antibodies also displayed normal SDC cellularity (data not shown). To investigate the role of NK cells, mice were treated with an anti-NK1.1 antibody every 3 d starting 3 d before B16F10 tumor injection. This resulted in profound loss of NK cells, but other changes in lymphocyte cellularity and tumor growth were limited (Supplementary Fig. 5e). However, mice depleted of NK cells had reduced frequencies of CD103⁺ SDCs in the TME, with no significant changes in the levels CD11b⁺ DCs (Fig. 3d). Consistent with our previous finding that T cell stimulation in tumors relies on tumor-resident CD103⁺ DCs, there was a trend toward reduced numbers of activated T cells in the tumors of mice lacking NK cells (Supplementary Fig. 5e). Interestingly, depletion of NK cells led to a small, but significant, decrease in the levels of CD103⁺ DCs in tumor draining and nondraining LN (Supplementary Fig. 5f), suggesting again that NK cells may play a more generalized role in controlling CD103⁺ DC levels in addition to their role in tumor. Taken as a whole, these findings suggest that, although both T cells and NK cells can produce *Flt3l* in tumor, the loss of T cells has no effect on tumor CD103⁺ DC levels, whereas *Flt3l* production by NK cells plays an important role in controlling the levels of these protective DCs in tumor.

NK cells make frequent and stable interactions with SDCs in the TME. NK cells are the dominant lymphocyte required for SDC levels in tumor. However, NK cells and SDCs are quite rare in tumor, thus we asked: how do NK cells exert control on SDCs in tumor? SDCs are only sparsely present in the TME compared to other APCs and interact infrequently with incoming T cells[3,4]. In contrast, when we undertook live two-photon slice imaging of B78 melanoma tumors, we found NK cells (marked by *Ncr1-GFP*) frequently arrested in close contact with SDCs (marked by an antibody against X-C motif chemokine receptor 1 (XCR1); Fig. 4a and Supplementary Video 1). After performing live intravital two-photon imaging of B78-cherryOVA tumors[14], which comprise B78 parental cells transfected with a mCherry–OVA fusion construct identical to that used in the PyMTChOVA mouse strain, we found approximately 1.9% of imaged NK cells could be found within 5 μm of a *Xcr1-Venus*⁺ cDC1, whereas only 0.38% of transferred MHC class I–restricted, ovalbumin-specific (OT-I) T cells can be found within 5 μm of a *Xcr1-Venus*⁺ cDC1 (Fig. 4b). Further, we observed

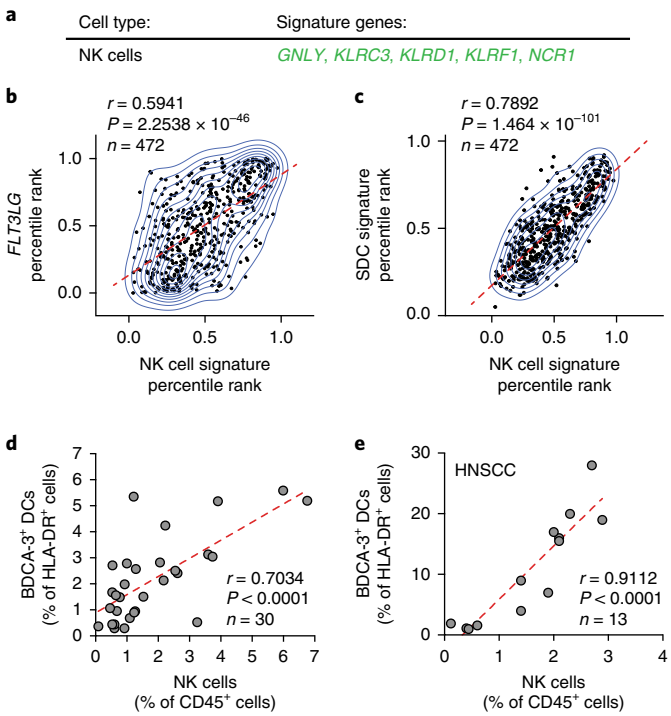

Fig. 5 | BDCA-3$^+$ DC levels correlate with levels of NK cells in the human melanoma TME. a, NK cell gene signature. **b**, *FLT3LG* expression normalized by percentile rank plotted versus the percentile rank of NK cell gene signature expression for individual patients in the TCGA melanoma dataset[11] ($n = 472$ biologically independent melanoma tumor samples). **c**, SDC gene signature (Fig. 1a) expression normalized by percentile rank versus the percentile rank of NK cell gene signature expression for individual patients in the TCGA melanoma dataset[11] ($n = 472$ biologically independent melanoma tumor samples). **d**, The frequency of NK cells among total CD45$^+$ cells versus the frequency of BDCA-3$^+$ DCs among total HLA-DR$^+$ cells for individual patients with melanoma in cohort A ($n = 30$ tumor samples from 29 patients). **e**, The frequency of NK cells among total CD45$^+$ cells versus the frequency of BDCA-3$^+$ DCs among total HLA-DR$^+$ cells for individuals in a cohort of patients with HNSCC ($n = 13$ biologically independent tumor samples). In **b**–**e**, each data point represents one sample, and the regression line (dashed red line) is superimposed. Correlation and two-tailed *P* value were assessed using the Pearson correlation coefficient and unpaired *t*-test.

migration (motion associated with substantial displacement) of NK cells greater than 5 µm from a XCR1$^+$ cDC1, whereas NK cells in close contact (< 5 µm) had reduced motility, consistent with continuous and/or synaptic engagements (Fig. 4c and Supplementary Video 2). These findings suggest that in tumor, NK cells are the most relevant source of FLT3L, which controls SDC levels, likely owing to an increased affinity of NK cells for cDC1 DCs. This finding is consistent with recent data showing chemokine–receptor pairing for NK cells and XCR1$^+$ DC in the TME[15]. Consistent with NK cells playing a direct role in DC survival, when CD103$^+$ DCs were sorted from WT mouse LNs and incubated with medium or purified NK cells, CD103$^+$ DCs that were cocultured with NK cells showed significantly increased survival over 24 h and 72 h of incubation (Fig. 4d). These studies suggest that NK cells, more often than T cells, form stable interactions with SDCs in tumor and that targeting NK cell levels may be a new therapy to increase FLT3L production and subsequently the levels or survival of SDCs in tumor. We note that, although we see evidence that NK cells provide increased survival to CD103$^+$ DCs in tumor, it is possible that NK cells may also be acting on DC precursors to control these SDCs.

Human NK cell abundance in tumor correlates with *FLT3LG* expression and BDCA-3$^+$ SDCs. Our mouse studies show that NK cells produce FLT3L and control the levels of SDCs in tumor. In light of these findings, we investigated human datasets for the abundance of NK cells by generating a NK cell gene signature based on previously published datasets and expression profiling of genes specific to NK cells[16,17] (Fig. 5a and Supplementary Fig. 6). Using the NK cell gene signature as an estimate of NK cell abundance in samples from the TCGA melanoma dataset[11], we found a significant correlation between the levels of NK cells in tumor and *FLT3LG* expression (Fig. 5b), consistent with intratumoral NK cells in humans being a source of FLT3LG. Consistent with the NK cell gene signature results (Fig. 5b), expression of natural cytotoxicity triggering receptor 1 (*NCR1*), a gene encoding a NK cell receptor expressed specifically in NK cells (Supplementary Fig. 6), showed a significant individual correlation with *FLT3LG* expression in tumor (Supplementary Fig. 7a). Furthermore, using gene signatures for SDCs (Fig. 1a) and NK cells (Fig. 5a) to estimate cellular abundance, we found a significant correlation between the levels of NK cells and SDCs in patients with melanoma (Fig. 5c), consistent with our mouse data. Expression of *NCR1*, a NK-specific gene, showed a significant individual correlation with the SDC signature (Supplementary Fig. 7b). To directly compare SDC and NK cell numbers, human melanoma biopsy samples were collected, digested into a single-cell suspension, and analyzed using flow cytometry (cohort A; Supplementary Fig. 2 and Supplementary Table 2). Direct analysis of NK cell and SDC populations in tumor revealed a significant correlation between the levels of NK cells and BDCA-3$^+$ DCs in tumor (Fig. 5d). BDCA-3$^+$ DCs in tumor did not correlate with levels of CD4$^+$ T helper (T_H) cells, CD8$^+$ T cells, or CD45$^-$ cells in tumor (Supplementary Fig. 7c–e), suggesting that this is a specific correlation between NK cells and BDCA-3$^+$ DCs. The correlation between NK cells and BDCA-3$^+$ DCs was also found in the TME of other cancer types, notably in head and neck squamous cell carcinoma (HNSCC; Fig. 5e), suggesting that this innate immune cell relationship may be broader than a single indication or subindication.

NK cells in human melanoma correlate with increased overall survival. A positive correlation of SDC and NK cells would logically predict that NK numbers should also predict survival. The NK cell gene signature (Fig. 5a), normalized in each patient as a *z* score, was used to bin patients with 'low' or 'high' NK cell numbers based on a median split (50% stringency). This revealed that patients with high NK cell numbers had a significantly increased OS in a Kaplan–Meier plot analysis of two independent datasets (Fig. 6a and Supplementary Fig. 7f)[11]. *NCR1* expression alone was significantly correlated with increased OS in the TCGA melanoma dataset[11]; furthermore, four of the five genes in the NK cell signature were individually associated with increased OS (Fig. 6b). These findings suggest, as we have shown in mouse models, that NK cells produce *FLT3LG* in patients with melanoma, controlling the levels of BDCA-3$^+$ stimulatory DCs in tumor and leading to increased patient survival. We note that these findings do not exclude a more traditional role for NK cells in tumor rejection, namely direct tumor cytolysis.

NK cells predict responsiveness to anti-PD-1 immunotherapy in patients with melanoma. Given the important role for NK cells in producing FLT3LG and controlling the levels of SDCs in tumor, which predict responsiveness to anti-PD-1 immunotherapy, we asked whether NK cells and/or T cells correlate with response to immunotherapy. We found no significant correlation between responsiveness to anti-PD-1 immunotherapy and T regulatory (T_{reg}) cells, CD4$^+$ T_H cells, CD8$^+$ T cells, and PD-1$^+$CTLA-4$^+$ T cells (Fig. 6c), although there were weak trends with some of these populations. In particular, we did not recapitulate previous data that

suggested that a PD-1$^+$CTLA-4$^+$CD8$^+$ 'exhausted' T cell signature was predictive of outcome. However, NK cells were significantly enriched in the tumors of patients that respond to anti-PD-1 immunotherapy (Fig. 6d). These findings are consistent with our finding in mice that NK cells, FLT3L, and SDCs form a cluster of determinants for outcome, likely at least in part driven by NK enhancement of SDC through production of FLT3L.

The NK–SDC axis is uniquely associated with responsiveness to anti-PD-1 immunotherapy. The comprehensive flow cytometry panels used for melanoma cohort A allowed for the quantification of 33 immune populations in the TME (Supplementary Fig. 2 and Supplementary Table 2). To determine whether NK cells and SDC levels in the TME are uniquely associated with responsiveness to anti-PD-1 immunotherapy, we assigned *z* scores to population fractions in each sample and found that, of identified immune cells in the TME, BDCA-3$^+$ DCs and NK cells significantly correlate with responsiveness to anti-PD-1 immunotherapy (Fig. 6e and Supplementary Table 3). Furthermore, when viewed this way, it appears that very high frequencies of HLA-DR$^-$CD4$^+$ T cells significantly correlate with anti-PD-1 responses and may represent an alternative prognostic feature of responsiveness in patients in whom BDCA-3$^+$ DCs and NK cells were not numerous. This may indicate that PD-1 blockade can be supported by more than one type of immune infiltrate, although further studies are required for confirmation.

Discussion

Here we identify a DC–NK cell contexture that correlates with the responsiveness of a patient to anti-PD1 immunotherapy in two independent cohorts. The idea that the non–T cell compartment would have a profound effect upon OS and response to T cell therapy is not in itself new, but this work specifically identifies an axis that connects one innate cell type (NK) to another APC subset (SDCs). This work also extends very recent work that shows NK cells produce cytokines in tumors that attract XCR1$^+$ DCs[15]. However, it takes this considerably further insofar as it provides the additional important fact that NK cells produce the formative cytokine for SDC, namely FLT3LG. In our study, frequencies of exhausted T cells themselves did not specifically predict response to therapy as was the case in previous studies[18]. At present, the source of this discrepancy is unclear, but may result from differences in digestion protocols; previous studies relied on long overnight digestion that may have differentially liberated or preserved these cells or raised these markers on activating T cells. In any case, given the finding that exhausted T cells are insensitive to restoration of function by anti-PD-1 immunotherapy[19], it is not immediately obvious how truly exhausted cells in vivo would then predict responsiveness; it is possible that the phenotype masquerades as exhaustion in some way. It is clear that more work is needed in this area, but both mouse and human data support the role for NK cells in making FLT3L, with the mouse studies unequivocally showing that NK cells play a major role in enhancing frequencies of SDCs in tumor. Whether this also occurs via interaction of NK cells with incoming pre-cDC precursors remains to be determined. Such experiments are expected to be difficult because of the low frequencies of each of the populations as well as the lack of available single-channel imaging reagents for live-imaging pre-cDC.

It also remains to be determined whether the NK–DC axis in tumor that defines responsiveness to anti-PD-1 immunotherapy has surrogates in the peripheral blood that may provide another more accessible readout of this population. A recent study has shown one marker to be upregulated in the peripheral blood of patients with metastatic melanoma that respond to anti-PD-1 immunotherapy is CD56, a marker associated with NK and NKT cells, and further suggest that a myeloid population in blood may be a good prognostic tool for identifying responsive patients[20]. Further studies are required to determine how these cell types relate to the NK–DC axis found in the TME, but these results suggest that there may be prognostic cell types in blood that represent a TME receptive to immunotherapy.

Both NK cell and SDC populations are routinely 'rare' at less than a few percent of total immune populations, yet this is an important dynamic range that predicts both OS as well as responsiveness to checkpoint blockade. Previous studies have implicated DC–NK interactions in activating NK cells in vitro, leading to better tumor responses in vivo[21,22]. In this study, we move our understanding of NK–DC interactions further and show direct NK–DC interactions in tumor in vivo. On the one hand, this may result from the aforementioned chemokine attraction between NK cells and SDCs[15], but on the other hand, it implies that these cells exist in special anatomical locations, perhaps akin to tertiary lymphoid structures. Although our imaging suggests much smaller 'clusters' of SDC with NK, it is formally possible that these clusters have additional features that we have not yet seen with imaging to date. We also note that T cells, although more abundant than NK cells and apparently

Fig. 6 | NK cell and BDCA-3$^+$ DC levels uniquely correlate with anti-PD-1 responsiveness in patients with melanoma. a, Kaplan–Meier plot of OS of patients with metastatic melanoma. Data from ref. [10] ($n=38$ biologically independent primary metastatic melanoma samples) are parsed into 'high' ($n=19$ biologically independent metastatic melanoma samples) and 'low' ($n=19$ biologically independent metastatic melanoma samples) bins at 50% (median) stringency thresholds for levels of expression of genes in the NK cell signature. The two-tailed *P* value was calculated using the log-rank test after adjusting for multiple comparisons using the Benjamini–Hochberg method. **b**, Left, Kaplan–Meier plot for OS of patients with melanoma median split for the gene expression of the NK cell–specific gene *NCR1*. Right, individual survival statistics associated with high expression of each gene in the NK cell gene signature. Data from ref. [11] ($n=454$ biologically independent melanoma patient samples) are parsed into 'high' ($n=227$ biologically independent melanoma samples) and 'low' ($n=227$ biologically independent melanoma samples) bins at 50% stringency threshold for levels of expression of *NCR1*, *KLRD1*, *GNLY*, *KLRC3*, or *KLRF1*. Plots and statistics were generated using the UZH TCGA Cancer Broswer[28]. Shaded regions mark the 95% confidence intervals, and the two-tailed *P* value was calculated using the log-rank test. **c**, Frequency of T cell populations (CD4$^+$ T_H, CD4$^+$ T_{reg}, and CD8$^+$ T cells) among all CD45$^+$ cells in tumors from individual patients. Patients were binned as responders (including partial or complete responses; $n=14$ biologically independent metastatic melanoma tumor samples) or nonresponders (including stable disease and progressive disease; $n=7$ biologically independent metastatic melanoma tumor samples). **d**, Percentage of NK cells among total CD45$^+$ cells in tumors from individual patients. Patients were binned as responders (including partial or complete responses; $n=14$ biologically independent metastatic melanoma tumor samples) or nonresponders (including stable disease and progressive disease; $n=9$ biologically independent metastatic melanoma tumor samples). In **c** and **d**, data are presented as mean ± s.e.m., with all individual points shown. Data were analyzed using the two-tailed unpaired parametric *t*-test. **e**, Heat map of 33 cell populations defined from flow cytometric analysis of a subset of melanoma samples from cohort A ($n=21$ biologically independent metastatic melanoma tumor samples from 20 patients) separated into anti-PD-1 responders (partial or complete responses; $n=14$ biologically independent samples) and nonresponders (stable and progressive disease; $n=7$ samples from 6 patients). For each population, two-tailed *P* values were calculated using the Wilcoxon rank-sum test. All populations are a fraction of total CD45$^+$ immune cells unless otherwise noted. Data for each row were logged and mean-centered; each column shows data from one sample.

similarly loaded with FLT3L, do not appear to be capable of driving SDC numbers, and this raises the question as to whether they might be blocked for production of the protein or if they simply do not have ample opportunity to interact with SDCs.

Prior to this work, it has long been thought that the predominant source of FLT3L is epithelial cells. This idea is traced to studies of in vitro elicted human vascular endothelial cells (HUVEC)[23], which likely are a uniquely elicited in vitro population whose in vivo correlate may not be obvious. Although our work does not negate the notion that FLT3L may be produced by epithelial cells, we find that the CD45$^-$ compartment shows no sizable *Flt3l* expression in tumors as compared to lymphocytes. It is also possible that epithelial cells

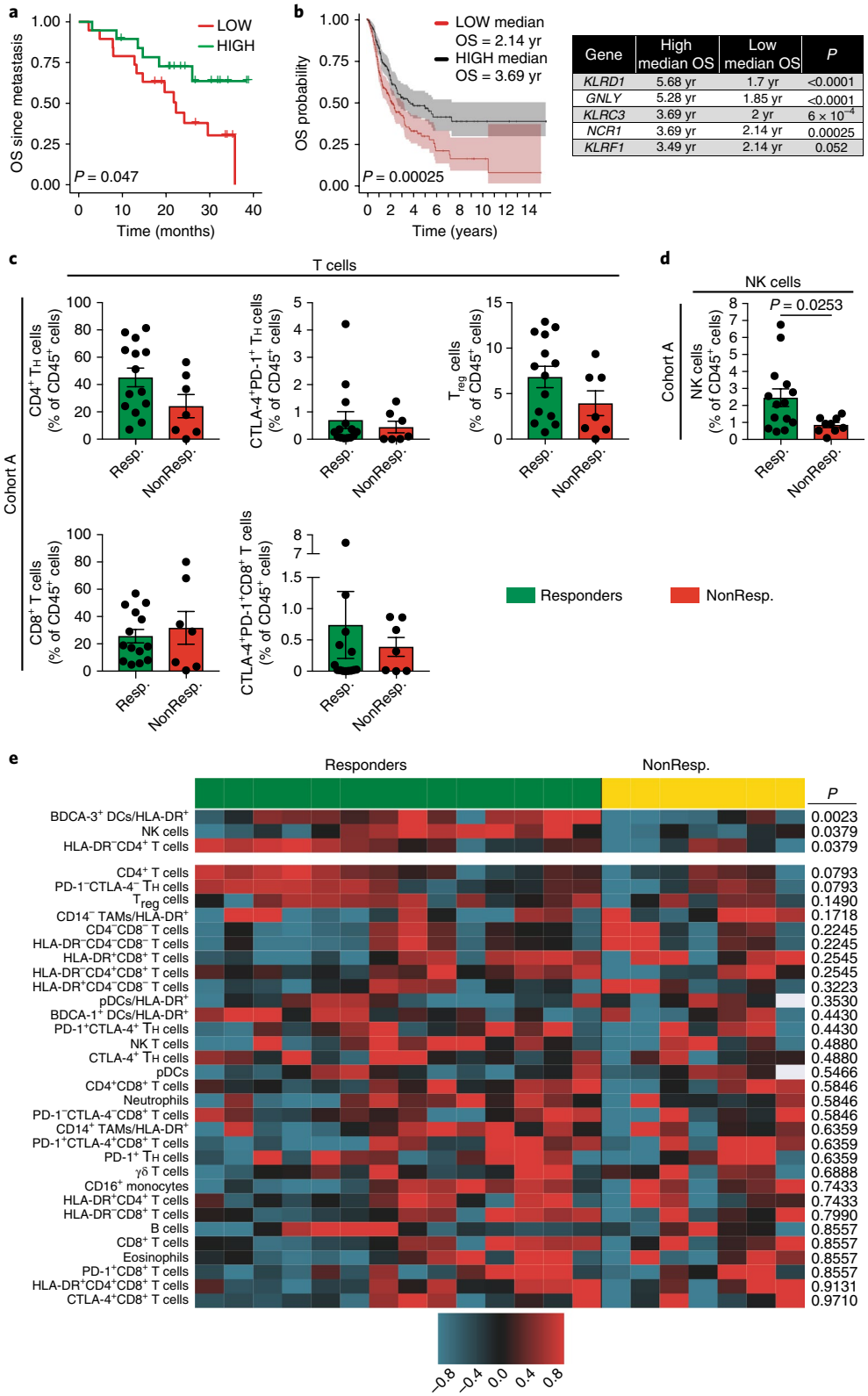

Gene	High median OS	Low median OS	P
KLRD1	5.68 yr	1.7 yr	<0.0001
GNLY	5.28 yr	1.85 yr	<0.0001
KLRC3	3.69 yr	2 yr	6×10^{-4}
NCR1	3.69 yr	2.14 yr	0.00025
KLRF1	3.49 yr	2.14 yr	0.052

in other tissue sites are more formidable sources of this cytokine. In accordance with this idea, work in mouse models suggests that nonhematopoietic cells are required to produce FLT3L in nonlymphoid tissues (lung, kidney, pancreas, and liver)[24]. Along similar lines, although NK cells are critical FLT3L producers in the TME, T cells may well be more important in other tissues or contexts.

It has long been acknowledged that NK cells can have a greater effect on tumors than their ability to kill cancer cells alone[21,25], but their role as critical producers of FLT3L and the formation of an apparently nonlytic interaction was not known. Our studies suggest that targeting NK cells either by increasing their numbers in the TME or by activating these cells should increase the levels of FLT3LG in tumor and in turn increase the levels of protective SDCs in the TME, either through skewed differentiation of precursor DCs in the tissue or prolonged survival of differentiated SDCs, providing increased responses to anti-PD-1 immunotherapy. Consistent with this idea, blocking CD96, an inhibitory receptor on NK cells and T cells[26,27], has been shown to increase NK cell activity and has recently been shown to work synergistically with anti-PD-1 and anti-CTLA-4 checkpoint blockade[26]. We predict that therapies aimed at recruiting and activating NK cells in tumors may prove to have orthogonal benefits to those provided by checkpoint inhibition.

Methods

Melanoma bioinformatics analysis. The melanoma dataset (gene expression omnibus (GEO) accession GSE19234 ($n=44$)[10]) was preprocessed by quantile normalizing in the R environment before evaluating the signature and assessing associations with survival (Cox proportional hazards). For NK gene signature analysis only, six secondary tumors were removed from the analysis of GSE19234, leaving 38 samples for analysis. The TCGA melanoma dataset downloaded from fireBrowse ($n=469$)[11] with RSEM-normalized expression data was further normalized by taking $\log_2(\text{Exp}+1)$ and z scoring across genes in R before evaluating the signature. The SDC:NSM ratio signature was calculated as the log of the mean expression of SDC genes divided by the mean expression of the NSM genes, followed by z score standardization (mean = 0, s.d. = 1). Survival analyses were performed using Cox proportional hazards modeling. Log-rank P values were used to assess significance after adjusting for multiple comparisons using the Benjamini–Hochberg method[29]. Kaplan–Meier survival plots were generated using the Survival package in R, and we classified each sample as 'high' or 'low' using the 33%, 50% (Median), or 66% value of the SDC or SDC:NSM ratio signature. Kaplan–Meier survival plots were generated for the NK cell gene signature using the Survival package in R and classified as 'high' or 'low' using a median split. The NK cell gene signature (Fig. 5a) was based on previously published differential expression analyses in peripheral lymphocytes[16,17] and further refined by selecting genes that were predominantly expressed in NK cells using the Primary Cell Atlas database from BioGPS[30] (Supplementary Fig. 6). Survival analysis with the NK cell gene signature was undertaken on median-normalized datasets (TCGA melanoma and metastatic melanoma). The NK cell gene signature was extracted from the dataset and used to calculate a median-based z score for each gene of the NK cell gene signature. z scores were then averaged across all signature genes for each patient, generating a one vector of means for each patient that was used to assess association with survival (Cox proportional hazards). Kaplan–Meier survival plots were generated using the Survival package in R, and we classified each sample as 'high' or 'low' using a median split (50% stringency), with gene signatures above the median classified as 'high' and below the median classified as 'low'.

Patients and samples. Patients were enrolled in this study if they had histologically confirmed stage III or IV unresectable metastatic melanoma. Patients provided written and informed consent to tissue collection under a University of California, San Francisco (UCSF) institutional review board (IRB)-approved protocol (UCSF Committee on Human Research (CHR) no. 13-12246). The study enrollment period occurred from December 2012 to November 2016, and the sample size was determined by the availability of specimens throughout this period. Patients were treated with the following monoclonal antibodies blocking the anti-PD-1–PDL-1 axis: pembrolizumab (Keynote 001, 002, 006 or expanded access program or commercial supply) or nivolumab (commercial supply).

Melanoma cohort A patient selection and sample collection. Cutaneous and subcutaneous metastatic melanomas (including metastases in the LN) were biopsied with either a punch (4 mm or 6 mm), a surgical excision, or core needle (16 g or 18 g) exclusively. Patients in cohort A ($n=33$ patients with $n=35$ samples) were selected without regard to prior treatment with immunotherapies; therefore, in this cohort, there is a range of patients from immunotherapy-naive to patients having been treated with anti-PD-1, ipilimumab, and/or IL-12 (Supplementary Table 2). Samples suspected to be the primary melanoma lesion are noted in Supplementary Table 2.

Melanoma cohort B patient selection and sample collection. Cutaneous and subcutaneous metastatic melanoma tumors were biopsied with either a punch (4 mm or 6 mm) or a surgical excision (sample K10), and all other tumor biopsies were with a core needle (16 g or 18 g) exclusively. An additional sample was sent for pathology evaluation. Biopsies ($n=23$) were collected before infusion of anti-PD-1 (Supplementary Table 2).

Evaluating responses to therapy. All response evaluation was performed through radiologic imaging and limited to the best overall response as defined by the Response Evaluation Criteria in Solid Tumors (RECIST) version 1.1. 'Complete Response' was defined as a complete regression of all target and nontarget lesions, 'Partial Response' was defined as lesions >30% regression of target with no new lesions appearing, 'Stable Disease' was defined as ≤30% decrease or ≤20% increase in the size of target lesions., and 'Progressive Disease' was defined as ≥20% increase in the size of target lesions or appearance of new lesions > 1 cm in size. Patients with complete or partial response were classified as 'responders', and those with stable disease or progressive disease were classified as 'nonresponders'. The associated clinical trial registration numbers (National Clinical Trial (NCT) Numbers) are: Protocol 01, NCT01295827; Protocol 02, NCT01704287; Protocol 06, NCT01866319; Expanded Access Program (EAP), NCT02083484. All clinical trials can be found at ClinicalTrials.gov.

Human tissue digestion. The fresh biopsy samples (cohort A and B) were immediately placed in a sterile container on saline-soaked gauze (or submerged in PBS) and placed in a container of wet ice for transport to the laboratory for evaluation. Cohort A tissue was vigorously minced with surgical scissors and transferred to a GenleMACs C Tube (Miltenyi Biotec) with 100 µg/mL Liberase TL (Roche) and 200 µg/mL DNase I (Roche) at 3 mL per gram of tissue. C tubes were incubated in the GentleMACS octo dissociator (Miltenyi Biotec) with heaters, following the manufacturers dissociation protocol (Miltenyi Biotec Tumor Dissociation Kit). 10 mL of sort buffer (PBS + 2% fetal calf serum (FCS) + 2 mM EDTA) was added to samples and filtered through a 100-µm filter and spun down, and red blood cells were lysed with 175 mM ammonium chloride. Cohort B tissue was vigorously minced with surgical scissors and transferred to a 50 mL conical with 20 µL/mL Liberase TL (at 5 mg/mL, Roche) and 50 U/ml DNase I (Roche) per 0.3 g of tissue for 30 min at 37° C with 5% CO_2 and constant agitation. Samples were then filtered through a 70-µm filter, spun down, and resuspended for staining[31].

Antibodies against human antigens. The following antibodies were used: CD45 clone Hl30 (eBioscience 47-0459-42), CD3e clone OKT3 (eBioscience 46-0037-42), HLA-DR clone L243 (eBioscience 48-9952-42), CD56 clone CMSSB (eBioscience 46-0567-42), CD56 clone HCD65 (BioLegend 318304), CD19 clone H1B19 (eBioscience 46-0198-42 and 56-0199-42), CD14 clone 61D3 (Invitrogen Q10056; Cohort 1), CD14 clone M5E2 (BioLegend 301836; Cohort 2), CD16 clone 3G8 (BioLegend 302040), CD11c clone 3.9 (eBioscience 56-0116-42), CD85g clone 17G10.2 (eBioscience 12-5179-42), BDCA-1 clone L161 (BioLegend 331516), BDCA-3 clone AD5-14H12 (Miltenyi 130-090-513), CD4 clone RPA-T4 (BioLegend 300550), CD8 clone RPA-T8 (BioLegend 301040), CD25 clone BC96 (BioLegend 302612), CD25 clone 2A3 (eBioscience 17-0259-42), FOXP3 clone PCH101 (eBioscience 77-5776-40), FOXP3 clone 236 A/E7 (eBioscience 25-4777-42), PD-1 clone EH-12 (BioLegend 329930), CTLA-4 clone BNI3 (BioLegend 369606), γδ T cell receptor (TCR) clone B1.1 (BioLegend 331212) and FLT3L (Abcam ab9688).

Flow cytometry. All antibodies were purchased from BD Pharmingen, eBioscience, Invitrogen, BioLegend, the UCSF hybridoma core, R&D Systems or Abcam, or they were produced in the Krummel Lab. For surface staining, cells were incubated with Fc receptor–blocking solution (Human, BioLegend 422301, Human TruStain FcX; Mouse, BioXCell BE0307, anti-CD16/32 antibody clone 2.4G2) and stained with antibodies in PBS + 2% FCS + 2 mM EDTA for 30 min on ice. Viability was assessed by staining with Zombie Aqua fixable viability dye (BioLegend, 423102) or Zombie NIR fixable viability dye (BioLegend 423106). All human samples were fixed with BD Cytofix before analysis, following the manufacturer's protocol. All mouse samples were run on the cytometer without fixation. For intracellular staining, samples were first stained for surface markers, as described above, and then fixed with fixation/permeabilization solution and washed with permeabilization buffer, per the manufacturer's suggested protocol (eBioscience 00-5523-00). Intracellular staining was undertaken in the presence of 2% FCS and an Fc receptor–blocking solution (BioLegend Human FcX). Flow cytometry was performed on a BD Fortessa or an Aria Fusion flow cytometer. Analysis of flow cytometry data was done using FlowJo (Treestar) software. For human flow cytometry data analysis, patient samples were coded, and flow analysis and outcome data were scored by separate individuals before data agglomeration. All human tumor samples were processed and analyzed using flow cytometry, but only those with at least 1,000 live $CD45^+$ cell events were included in the analysis. It should be noted that although CD85g is a strong marker for pDCs in peripheral blood, it can provide low signal on tissue pDCs, meaning that the use of this marker to define pDCs in tumor may underrepresent the actual pDC population in tumor.

Bioinformatic analysis of human flow cytometry data. Myeloid and lymphoid populations in tumor were defined as shown in Supplementary Fig. 2. For each population, the Wilcoxon rank-sum test statistic, *P* value and *q* value were calculated between responders and nonresponders. Wilcoxon rank-sum test statistics and *P* values were calculated using the wilcox.exact function from the exactRankTests R package, and *q* values were calculated using the *q* value function in the Bioconductor R package. A heat map of population frequency out of total $CD45^+$ or $HLA\text{-}DR^+$ cells (as indicated) was made using the clustermap method from the seaborn python module. The population frequency data was logged and mean-centered. Row and column clustering were suppressed when generating the heat map, and instead rows were ordered by the calculated *P*, and the columns were ordered by responder status.

RNA sequencing analysis of human melanoma samples. With a subset of melanoma samples from patients in cohort A, 50,000 total live cells, as determined by staining with the Zombie Aqua fixable viability dye (BioLegend 423102), were directly sorted into lysis buffer by fluorescence-activated cell sorting (FACS) to isolate RNA. RNA was isolated using the Dynabeads mRNA DIRECT purification kit (ThermoFisher Scientific 61011), per the manufacturer's suggested protocol. Isolated RNA was converted into amplified cDNA using the Ovation RNA-Seq System V2 kit (NuGen 7102-A01), and cDNA was converted into RNA-seq libraries using the Nextera XT DNA Library Prep kit (Illumina FC-131-2001), following the manufacturer's suggested protocol. RNA-seq library quality was checked using a Bioanalyzer HS DNA chip (Agilent) and pooled. Pooled libraries were then sequenced via a single-read 50-bp MiSeq (Illumina) run, and libraries containing > 10% of reads aligned to coding regions and > 1,000 unique reads in the total library were selected for further sequencing. RNA-seq libraries that met the previous quality control criteria were pooled and submitted to the UCSF Center for Advance Technology for paired-end, 100-bp (PE100) sequencing on the HiSeq4000 (Illumina). Using the Burrows–Wheeler Aligner[32], we aligned sequenced RNA-seq library reads against a reference of ribosomal RNA (rRNA) and mitochondrial RNA (mtRNA) to deplete the dataset of rRNA and mtRNA. The remaining reads were then aligned to the Ensembl GrCh38.85 transcriptome build using the software package RSEM[33] with the alignment tool Bowtie 2 (ref. [34]). RNA-seq libraries with $> 1 \times 10^6$ protein-coding, non-rRNA read counts were used to analyze RNA expression. Transcripts per million (TPM) for individual genes were used for analyses, and in all cases, TPMs were normalized by *z* score. When gene signatures were calculated from these RNA-seq datasets, the TPM of each individual gene in the signature was normalized by calculating a *z* score, and then the *z* scores were averaged for the entire signature to give the final gene signature *z* score.

Mouse strains. All mice were housed and bred at UCSF and were maintained under specific pathogen-free conditions in accordance with the regulatory standards of the National Institutes of Health (NIH) and American Association of Laboratory Animal Care standards and that were consistent with the UCSF Institution of Animal Care and Use Committee (IACUC approval no. AN170208-01B). C57Bl/6 (WT) mice were purchased from The Jackson Laboratory or Simonsen Laboratories or were bred in house. Age-matched and sex-matched animals were used for all experiments. Ectopic tumor experiments used 6- to 8-week-old animals. The *Flt3l*$^{-/-}$ (ref. [35]), *Il2rg*$^{-/-}$ (ref. [36]), *Ncr1-GFP*[37], *actin-CFP*[38], and OT-I transgenic[39] mouse strains were purchased from The Jackson Laboratory. *Ncr1-GFP* mice were used as heterozygous animals, as the knock-in disrupts gene expression. *Xcr1-Venus*[40] and *Cd11c-mCherry* mice[41] were bred at UCSF. The *Flt3l*-reporter mice were generated under contract by the company Biocytogen. The P2A-*cre-ER*^{T2}-T2A-*TFP* sequence was inserted between exon 8 and the 3′-UTR of *Flt3l* at the endogenous locus using CRISPR–Cas9 targeting. Proper insertion of the reporter construct was confirmed through PCR and DNA sequencing. Genotyping of *Flt3l*-reporter mice was done via PCR using a common forward primer that binds in the *Flt3l* locus (5′-AAGGAGTCCCATAGCCCTAGAAGCC-3′), a WT reverse primer that binds in the *Flt3l* gene (5′-CTCCACAG CTTACGATTGTCGGAGC-3′), and a knock-in reverse primer specific to the *cre-ER*^{T2} knock-in (5′-CCTGTCCCTGAACATGTC CATCAG-3′). *Flt3l*-reporter mice were crossed onto the spontaneous tumor model PyMTChOVA background[14], and offspring were screened for the *PyMTchOVA* transgene and the *Flt3l*-reporter knock-in through PCR. Female PyMTChOVA; *Flt3l*-reporter animals were monitored for tumors and used at 20–30 weeks of age.

Determination of FLT3L serum levels. Blood from *Flt3l*-reporter homozygous mice, WT C57Bl/6 mice, or C57Bl/6 mice bearing

2-week-old B16F10 tumors was collected from the tail vein or by cardiac puncture and allowed to sit for 2 h at room temperature to clot. Blood was centrifuged for 20 min at 2,000 *g*, and serum was collected. Serum was diluted 1:1 with PBS, and FLT3L levels were determined through ELISA using the Quantikine ELISA kit (R&D Systems), per the manufacturer's suggested protocol.

Cell lines and cell culture. The following tumor cell lines were cultured under standard conditions before injection into mice: B16-F10 (ref. [42]), B78-parental[43], B78-cherryOVA[14], and MC38 (ref. [44]). Cells were cultured at 37 °C and 5% CO_2 in DMEM plus 10% FCS with 1% penicillin–streptomycin–glutamine on tissue culture–treated plastic plates and split every other day.

Ectopic tumor injection. Tumor cell lines were harvested and washed three times with PBS, then mixed at a 1:1 ratio with growth factor–reduced Matrigel Matrix (BD Biosciences) for a final injection volume of 50 µL. 1.5×10^5 B16F10 and B78 tumor cells were injected in the left flank of shaved mice subcutaneously and allowed to grow for 14 d before use, unless otherwise stated.

Mouse tissue digestion. Tumors were dissected from mice, and the total weight of removed tumor tissue was determined. Tumors were then minced using scalpels and digested with 500 U/mL Collagenase IV (Sigma), 100 U/mL Collagenase I (Worthington), and 200 µg/mL DNAse I (Roche) per 0.3 g of tumor weight for 30 min in a 50-mL conical tube at 37 °C with constant shaking. After 30 min, 7 mL of PBS + 2% FCS + 2 mM EDTA was added to the tubes, and tumors were passed through a 100-µm cell strainer to remove large pieces of tumor. Large pieces of tumor were dissociated by pushing the cells through the 70-µm cell strainer with the plunger of a 5-mL syringe. Subcutaneous tumors drained to the inguinal, axillary, and brachial skin-draining LNs. Therefore, the inguinal, axillary, and brachial LNs were harvested for tumor draining LNs. For digestion, LNs were carefully dissected from mice and cleaned of fat. LNs were pierced and torn with sharp forceps in 24-well plates and incubated for 15 min at 37 °C in 1 mL of digestion buffer (100 U/mL collagenase I, 500 U/mL collagenase IV, and 200 µg/mL DNAse I in RPMI-1640). After the first 15 min of incubation, cells were pipetted up and down repeatedly and then returned for a second 15-min incubation at 37 °C. After digestion, LNs were washed with PBS + 2% FCS + 2 mM EDTA and filtered through a 100-µm cell strainer before staining for flow cytometry.

Antibodies against mouse antigens. The following antibodies were used: CD3 clone 17A2 (BioLegend 100237 and 100244), CD4 clone RM4-5 (BioLegend 100545 and 100510), CD4 clone GK13 (BioLegend 100403), CD8 clone 53-6.7 (BioLegend 100734), CD11b clone M1/70 (BioLegend 101257), CD11c clone N418 (BioLegend 117339 and 117338), CD19 clone 6D5 (BioLegend 115522), CD24 clone M1/69 (BioLegend 101822), CD45 clone 30-F11 (BioLegend 103139, 103132, and 103114; eBioscience 56-0451-82), CD45R clone RA3-6B2 (BioLegend 103247, 103246, and 103226), CD69 clone H1.2F3 (eBioscience 25-0691-81), CD90.2 clone 30-H12 (BioLegend 105331), CD103 clone 2E7 (BioLegend 121406 and 121414), F4/80 clone BM8 (BioLegend 123108), Flt3L (R&D Systems AF427), Ly6C clone HK1.4 (BioLegend 128037), Ly6G clone 1A8 (BioLegend 127645), MHC-II clone M5/114.15.2 (BioLegend 707631), NK1.1 clone PK136 (BioLegend 108707, 108720, and 108749), streptavidin–Brilliant Violet 650 (BioLegend 405231), and streptavidin–APC (eBioscience 17-4317-82). These depleting antibodies were used: NK1.1 clone PK136 (BioXCell BE0036) and IgG2a isotype control (BioXCell BE0085).

Isolation of CD103⁺ DCs and NK cells and in vitro coculture. To isolate CD103⁺ DCs, all non-gut draining LNs were harvested from wild-type C57Bl/6J mice and dissociated into a single-cell culture via digestion at 37 °C in 1 mL of 500 U/mL Collagenase IV (Sigma), 100 U/mL Collagenase I (Worthington), and 200 µg/mL DNAse I (Roche) for 30 min with agitation every 15 min. Single-cell LN suspensions were stained with a biotin-conjugated anti-CD2 antibody (BioLegend 100104), and negative selection was performed with an EasySep Biotin Selection Kit following the manufacturer's instructions before staining. CD103⁺ DCs were sorted using the gating scheme described in Supplementary Fig. 3e. 1×10^4 CD103⁺ DCs were incubated with 1×10^5 NK cells isolated using the EasySep Mouse NK Cell Isolation Kit, per the manufacturer's instructions. NK cells and CD103⁺ DCs were cocultured in RPMI + 10% FCS + 1% penicillin–streptomycin–glutamine + 1 × nonessential amino acids + 50 µM β-mercaptoethanol + 7.5 ng/mL recombinant murine granulocyte-macrophage colony–stimulating factor (GM-CSF). Cells were isolated at 24 or 72 h postincubation, and viability was assessed through staining with Zombie NIR fixable viability dye (BioLegend 423106). CD103⁺ DCs were gated as described in Supplementary Fig. 3e.

Ex vivo tumor slice staining and multiphoton imaging. All imaging was performed using a custom-built two-photon setup equipped with two infrared lasers (MaiTai: Spectra Physics; Chameleon: Coherent). Emitted light was detected using a 25 × 1.2-NA water lens (Zeiss) coupled to a six-color detector array (custom; using Hamamatsu H9433MOD detectors), and alternating laser excitation was used to yield 12 detection channels. The emission filters used were: violet 417/50, blue 475/23, green 510/42, yellow 542/27, red 607/70, far red 675/67. The microscope was controlled by the MicroManager software suite[45], and *z*-stack images were acquired with 20-fold averaging and *z*-depths of 5 µm. Data analysis was performed using the Imaris software suite (Bitplane).

Ncr1-GFP animals with 2-week-old ectopic melanoma tumors were euthanized, and tumors were harvested. Obstructing fat was removed, and tumors were embedded in 4% low-melting agarose in PBS (SeaPlaque, Lonza). Sections with a thickness of 300 µm thick were prepared using a Compresstome VF-200 (Precisionary Instruments Inc.) tissue slicer. Slices were stained with Brilliant Violet 421 anti-XCR1 antibody clone ZET (BioLegend 148216) and Brilliant Violet 605 anti-CD45 antibody clone 30-F11 (BioLegend 103139) in RPMI-1640 supplemented with 5% rat serum for 2 h at 37 °C with 5% CO_2. Slices were washed in RPMI-1640 and attached to plastic coverslips using Vetbond (3 M). Slices were kept at 37 °C with constant flow-over of RPMI-1640 (without phenol red) with CO_2 bubbled in throughout imaging. The MaiTai laser was tuned to 800 nm for excitation of the BV421 and BV605 fluorophores. The chameleon laser excitation was tuned to 910 nm for excitation of GFP.

For quantification of T cell and NK cell distances to XCR1⁺ DCs, *Xcr1-Venus*; *Ncr1-GFP*; *Cd11c-mCherry* triple-reporter mice were injected with 2×10^4 *actin-CFP* OT-I CD8⁺ T cells into the tail vein 1 d before tumor injection. Mice were injected with150,000 B78 chOVA tumor cells in the absence of growth factor-reduced Matrigel Matrix and intravital imaging of tumors was performed 2 weeks later. Still 3D projections of tumors were used to calculate distances. T cell–DC and NK cell–DC distances were measured using the Imaris software suite (Bitplane). Briefly, the center of each cell type was determined, and the smallest distance between the cell types of interest (T cell–DC or NK cell–DC) was calculated using the equation:

$$R = \sqrt{(x_{\text{cell1}} - x_{\text{cell2}})^2 + (y_{\text{cell1}} - y_{\text{cell2}})^2 + (z_{\text{cell1}} - z_{\text{cell2}})^2}$$

With *R* being the distance between the two cells, and *x*, *y*, and *z* representing the coordinates of the cells in the 3D space. Three separate

image frames from two independent tumors were used to calculate the percentage of T cells and NK cells within 5 µm of a XCR1$^+$ DC. For imaging, the MaiTai laser was tuned to 810 nm for excitation of CFP, and the chameleon laser excitation was tuned to 980 nm for excitation of Venus, mCherry, and GFP. *z*-stack images were acquired with 15-fold averaging and *z*-depths of 4µm.

Bone marrow chimera generation. To generate BM chimeras, we lethally irradiated *Flt3l*$^{-/-}$ mice via exposure to 1,100 rads of irradiation in two doses, 3 h apart. 2×10^6–5×10^6 BM cells, consisting of 50% *Il2rg*$^{-/-}$ and 50% WT or *Flt3l*$^{-/-}$ BM were injected retro-orbitally to reconstitute irradiated mice. Chimeric mice were injected with subcutaneous B16F10 tumor cells 8 weeks after reconstitution.

Tumor measurements. For tumor measurements, tumor area (mm^2) was measured with calipers as tumor width × tumor height over the indicated time periods.

Statistical analysis. Statistical analyses were performed using GraphPad Prism software. Normality of data was assessed using the D'Agostino–Pearson omnibus normality test in Prism, and all data presented passed the normality assumption unless described otherwise. Unless specifically noted, all data are representative of >3 independent experiments. Data are shown as mean ± s.e.m., calculated using Prism, unless otherwise noted. Specific statistical tests used were paired and unpaired parametric *t*-tests or unpaired nonparametric Mann–Whitney U test (if data failed normal assumption), and $P<0.05$ was considered statistically significant.

Reporting Summary. Further information on experimental design is available in the Nature Research Reporting Summary linked to this article.

Data availability. All RNA-seq reads were uploaded to GEO with accession number GSE113126. All other relevant data are available from the corresponding author on request.

Methods

Methods, including statements of data availability and any associated accession codes and references, are available at https://doi.org/10.1038/s41591-018-0085-8.

Received: 6 February 2018; Accepted: 4 May 2018;
Published online: 25 June 2018

References

1. Topalian, S. L., Drake, C. G. & Pardoll, D. M. Immune checkpoint blockade: a common denominator approach to cancer therapy. *Cancer Cell.* **27**, 450–461 (2015).
2. Rizvi, N. A. et al. Mutational landscape determines sensitivity to PD-1 blockade in non–small cell lung cancer. *Science* **348**, 124–128 (2015).
3. Broz, M. L. et al. Dissecting the tumor myeloid compartment reveals rare activating antigen-presenting cells critical for T cell immunity. *Cancer Cell.* **26**, 638–652 (2014).
4. Salmon, H. et al. Expansion and activation of CD103$^+$ dendritic cell progenitors at the tumor site enhances tumor responses to therapeutic PD-L1 and BRAF inhibition. *Immunity* **44**, 924–938 (2016).
5. Sánchez-Paulete, A. R. et al. Cancer immunotherapy with immunomodulatory anti-CD137 and ant-PD-1 monoclonal antibodies requires BATF3-dependent dendritic cells. *Cancer Discov.* **6**, 71–79 (2016).
6. Hildner, K. et al. Batf3 deficiency reveals a critical role for CD8$^{\alpha+}$ dendritic cells in cytotoxic T cell immunity. *Science* **322**, 1097–1100 (2008).
7. Spranger, S., Dai, D., Horton, B. & Gajewski, T. F. Tumor-residing Batf3 dendritic cells are required for effector t cell trafficking and adoptive T cell therapy. *Cancer Cell.* **31**, 711–723.e4 (2017).
8. Lavin, Y. et al. Innate immune landscape in early lung adenocarcinoma by paired single-cell analyses. *Cell* **169**, 750–765.e17 (2017).
9. Spranger, S., Bao, R. & Gajewski, T. F. Melanoma-intrinsic β-catenin signalling prevents anti-tumor immunity. *Nature* **523**, 231–235 (2015).
10. Bogunovic, D. et al. Immune profile and mitotic index of metastatic melanoma lesions enhance clinical staging in predicting patient survival. *Proc. Natl. Acad. Sci. USA* **106**, 20429–20434 (2009).
11. Cancer Genome Atlas Network. Genomic classification of cutaneous melanoma. *Cell* **161**, 1681–1696 (2015).
12. Wei, S. C. et al. Distinct cellular mechanisms underlie anti-CTLA-4 and anti-PD-1 checkpoint blockade. *Cell* **170**, 1120–1133.e17 (2017).
13. Liu, K. & Nussenzweig, M. C. Origin and development of dendritic cells. *Immunol. Rev.* **234**, 45–54 (2010).
14. Engelhardt, J. J. et al. Marginating dendritic cells of the tumor microenvironment cross-present tumor antigens and stably engage tumor-specific T cells. *Cancer Cell.* **21**, 402–417 (2012).
15. Böttcher, J. P. et al. NK cells stimulate recruitment of cDC1 into the tumor microenvironment promoting cancer immune control. *Cell* **172**, 1022–1037.e14 (2018).
16. Du, X. et al. Genomic profiles for human peripheral blood T cells, B cells, natural killer cells, monocytes, and polymorphonuclear cells: comparisons to ischemic stroke, migraine, and Tourette syndrome. *Genomics* **87**, 693–703 (2006).
17. Bezman, N. A. et al. Molecular definition of the identity and activation of natural killer cells. *Nat. Immunol.* **13**, 1000–1009 (2012).
18. Loo, K. et al. Partially exhausted tumor-infiltrating lymphocytes predict response to combination immunotherapy. *JCI Insight* **2**, 93433 (2017).
19. Philip, M. et al. Chromatin states define tumour-specific T cell dysfunction and reprogramming. *Nature* **545**, 452–456 (2017).
20. Krieg, C. et al. High-dimensional single-cell analysis predicts response to anti-PD-1 immunotherapy. *Nat. Med.* **24**, 144–153 (2018).
21. Zitvogel, L. Dendritic and natural killer cells cooperate in the control/switch of innate immunity. *J. Exp. Med.* **195**, F9–F14 (2002).
22. Fernandez, N. C. et al. Dendritic cells directly trigger NK cell functions: cross-talk relevant in innate anti-tumor immune responses in vivo. *Nat. Med.* **5**, 405–411 (1999).
23. Solanilla, A. et al. Expression of Flt3-ligand by the endothelial cell. *Leukemia* **14**, 153–162 (2000).
24. Miloud, T., Fiegler, N., Suffner, J., Hämmerling, G. J. & Garbi, N. Organ-specific cellular requirements for in vivo dendritic cell generation. *J. Immunol.* **188**, 1125–1135 (2012).
25. Goding, S. R., Yu, S., Bailey, L. M., Lotze, M. T. & Basse, P. H. Adoptive transfer of natural killer cells promotes the anti-tumor efficacy of T cells. *Clin. Immunol.* **177**, 76–86 (2017).
26. Blake, S. J. et al. Suppression of metastases using a new lymphocyte checkpoint target for cancer immunotherapy. *Cancer Discov.* **6**, 446–459 (2016).
27. Dougall, W. C., Kurtulus, S., Smyth, M. J. & Anderson, A. C. TIGIT and CD96: new checkpoint receptor targets for cancer immunotherapy. *Immunol. Rev.* **276**, 112–120 (2017).
28. Cheng, P. F., Dummer, R. & Levesque, M. P. Data mining The Cancer Genome Atlas in the era of precision cancer medicine. *Swiss Med. Wkly.* **145**, w14183 (2015).
29. Benjamini, Y. & Hochberg, Y. Controlling the false discovery rate: a practical and powerful approach to multiple testing. *J. R. Stat. Soc. Ser. B Stat. Methodol.* **57**, 289–300 (1995).
30. Wu, C., Jin, X., Tsueng, G., Afrasiabi, C. & Su, A. I. BioGPS: building your own mash-up of gene annotations and expression profiles. *Nucleic Acids Res.* **44** D1, D313–D316 (2016).
31. Ruffell, B. et al. Leukocyte composition of human breast cancer. *Proc. Natl. Acad. Sci. USA* **109**, 2796–2801 (2012).
32. Li, H. & Durbin, R. Fast and accurate short read alignment with Burrows–Wheeler transform. *Bioinformatics* **25**, 1754–1760 (2009).
33. Li, B. & Dewey, C. N. RSEM: accurate transcript quantification from RNA-seq data with or without a reference genome. *BMC Bioinforma.* **12**, 323 (2011).
34. Langmead, B. & Salzberg, S. L. Fast gapped-read alignment with Bowtie 2. *Nat. Methods* **9**, 357–359 (2012).
35. McKenna, H. J. et al. Mice lacking flt3 ligand have deficient hematopoiesis affecting hematopoietic progenitor cells, dendritic cells, and natural killer cells. *Blood* **95**, 3489–3497 (2000).
36. Cao, X. et al. Defective lymphoid development in mice lacking expression of the common cytokine receptor γ chain. *Immunity* **2**, 223–238 (1995).
37. Gazit, R. et al. Lethal influenza infection in the absence of the natural killer cell receptor gene *Ncr1*. *Nat. Immunol.* **7**, 517–523 (2006).
38. Hadjantonakis, A.-K., Macmaster, S. & Nagy, A. Embryonic stem cells and mice expressing different GFP variants for multiple non-invasive reporter usage within a single animal. *BMC Biotechnol.* **2**, 11 (2002).
39. Hogquist, K. A. et al. T cell receptor antagonist peptides induce positive selection. *Cell* **76**, 17–27 (1994).
40. Yamazaki, C. et al. Critical roles of a dendritic cell subset expressing a chemokine receptor, XCR1. *J. Immunol.* **190**, 6071–6082 (2013).

41. Khanna, K. M. et al. T cell and APC dynamics in situ control the outcome of vaccination. *J. Immunol.* **185**, 239–252 (2010).
42. Fidler, I. J. Biological behavior of malignant melanoma cells correlated to their survival in vivo. *Cancer Res.* **35**, 218–224 (1975).
43. Graf, L. H. Jr., Kaplan, P. & Silagi, S. Efficient DNA-mediated transfer of selectable genes and unselected sequences into differentiated and undifferentiated mouse melanoma clones. *Somat. Cell. Mol. Genet.* **10**, 139–151 (1984).
44. Corbett, T. H., Griswold, D. P. Jr., Roberts, B. J., Peckham, J. C. & Schabel, F. M. Jr. Tumor induction relationships in development of transplantable cancers of the colon in mice for chemotherapy assays, with a note on carcinogen structure. *Cancer Res.* **35**, 2434–2439 (1975).
45. Pinkard, H., Stuurman, N., Corbin, K., Vale, R. & Krummel, M. F. Micro-Magellan: open-source, sample-adaptive, acquisition software for optical microscopy. *Nat. Methods* **13**, 807–809 (2016).

Acknowledgements

We thank L. Lanier, J. Roose and L. Fong for advice, and we thank M. Spasic and N. Khurana for support with response data. This work was supported by National Institutes of Health (NIH) grant R01CA197363, awarded to M.F.K. Acquisition and processing of human melanoma samples in cohort A described in this study was funded in part by contributions from AbbVie, Amgen, and Bristol-Myers Squibb as members of the Immunoprofiler Consortium. Further support came from NIH grant 5P30CA082103, awarded to the University of California, San Francisco (UCSF) Hellen Diller Family Comprehensive Cancer Center. M.B. was supported by the Genentech Predoctoral Research Fellowship, the Margaret A. Cunningham Immune Mechanisms in Cancer Research Fellowship Award, and the Achievement Reward for College Scientists Scholarship. K.C.B. was supported by a postdoctoral fellowship from the Cancer Research Institute and Fibrolamellar Cancer Foundation.

Author contributions

K.C.B. designed and performed the experiments and wrote and edited the manuscript. J.H. assisted in analysis of tumor-infiltrating myeloid populations and data analysis. M.L.B. designed and performed experiments with melanoma cohort B. F.J.C. assisted in imaging data analysis. M.B. assisted in analysis of tumor-infiltrating myeloid populations and T cell–depletion experiments. A.J.C. assisted in analysis of HNSCC tumor samples. R.K. and A.E.N. assisted in analysis of tumor-infiltrating myeloid populations. K.L. and A.I.D. provided human melanoma biopsies, clinical data, and edited the manuscript. M.D.R. read the manuscript and provided useful discussion. M.D.A. provided human melanoma biopsies and clinical data. D.B. and N.B. provided metastatic melanoma data, and D.B. edited the manuscript. D.M.W. performed statistical analyses. P.K.H and W.R.R provided human HNSCC samples. J.L.P., B.S., and S.A. provided bioinformatics analyses. V.C. managed sample collection, assisted in analysis of tumor-infiltrating myeloid populations, read the manuscript, and provided useful discussion. M.F.K. conceived the project and wrote and edited the manuscript.

Competing interests

J.L.P. was an employee at Pionyr Immunotherapeutics at the time of manuscript writing. The other authors declare no competing interests.

Additional information

Supplementary information is available for this paper at https://doi.org/10.1038/s41591-018-0085-8.

Reprints and permissions information is available at www.nature.com/reprints.

Correspondence and requests for materials should be addressed to M.F.K.

Publisher's note: Springer Nature remains neutral with regard to jurisdictional claims in published maps and institutional affiliations.

nature research

Corresponding author(s): Matthew F. Krummel

☐ Initial submission ☐ Revised version ☒ Final submission

Life Sciences Reporting Summary

Nature Research wishes to improve the reproducibility of the work that we publish. This form is intended for publication with all accepted life science papers and provides structure for consistency and transparency in reporting. Every life science submission will use this form; some list items might not apply to an individual manuscript, but all fields must be completed for clarity.

For further information on the points included in this form, see Reporting Life Sciences Research. For further information on Nature Research policies, including our data availability policy, see Authors & Referees and the Editorial Policy Checklist.

Experimental design

1. Sample size

Describe how sample size was determined.

Power calculations were used to determine the number of animals used in these studies. Human cohort sample sizes were dependent on the number of patient samples received within the collection period. As we were interested in understanding if BDCA3+ DCs (SDCs) correlate with responsiveness to anti-PD-1 immunotherapy, which had never been determined, we used Power Calculations after collecting samples to determine the statistical power in our cohorts. Given the parameters in cohort A we have a 100% power calculation with this sample size and given the parameters of cohort B we had a 100% power calculation. These findings suggest that the human cohort sizes used in this study are sufficient.

2. Data exclusions

Describe any data exclusions.

Given the variability of human melanoma sample size, for some samples only a subset of antibody stains could be undertaken. Therefore, in certain analyses of human cohort A only subsets of samples were used due to a lack of data (e.g. lack of RNA sequencing or the lack of a flow cytometry antibody stain panel).

For the NK gene signature survival analysis 6 secondary tumors were removed from the analysis of GSE19234 dataset.

In the experiments depicted in Figure 3b and Supplementary Figure 5b-c some samples were excluded due to technical issues (insufficient cells for all staining panels and/or corrupted data file).

In the experiments depicted in Figure 3D and Supplementary Figure 5e-f some samples were excluded for technical reasons (either insufficient cells to complete all stain panels or a corrupted data file); isotype treated lymphocyte populations have n=9 and NK-depleted myeloid cells have n=9 as each group had one sample that was not analyzed for technical reasons.

3. Replication

Describe whether the experimental findings were reliably reproduced.

Experimental findings were reliably reproduced.

4. Randomization

Describe how samples/organisms/participants were allocated into experimental groups.

All human response evaluation was with radiologic imaging and limited to best overall response using the Response Evaluation Criteria in Solid Tumors version 1.1 (RECIST). Complete Response was defined as a complete regression of all target and non-target lesions, Partial Response was defined as regression of target lesions > 30 % with no new lesions appearing, Stable disease was defined as ≤ 30 % decrease or ≤ 20 % increase in the size of target lesions. Progressive disease was defined as increases in target lesions ≥ 20 % or appearance of new lesions > 1 cm in size. Patients with complete or partial response were classified as “responders” while those with stable disease or progressive disease were classified as “non-responders”.

In antibody treated (NK cell or T cell depletion) animals, isotype treated and

depleted animals were co-housed in cages and animals were randomly assigned to treatment or control groups.

For mixed bone marrow chimera experiments animals were randomly selected for the genotype of bone marrow transferred. All chimeras were co-housed with all possible bone marrow genotypes.

Whenever possible control and treated animals were co-housed to avoid confounding effects. For mutant experiments (Il2rg–/–, Rag–/–) there was no way to randomly select animals as these mutant animals are kept as homozyygous lines. However, these samples were analyzed by gating on control (WT) samples first and then transferring the exact same gates to the mutant animal samples.

5. Blinding

Describe whether the investigators were blinded to group allocation during data collection and/or analysis.

Patient anti-PD-1 responder status was blinded prior to analysis of immune populations of the tumor microenvironment in human melanoma samples.

Animal genotypes during data acquisition and analysis was not blinded. In these studies that gating of flow cytometric data was undertaken in such a way that gates were drawn on control (WT) samples and then exactly duplicated onto the mutant or treated animals. In this way the samples were consistently gated without the need for blinding the samples.

Note: all studies involving animals and/or human research participants must disclose whether blinding and randomization were used.

6. Statistical parameters

For all figures and tables that use statistical methods, confirm that the following items are present in relevant figure legends (or in the Methods section if additional space is needed).

n/a	Confirmed
☐	☒ The exact sample size (*n*) for each experimental group/condition, given as a discrete number and unit of measurement (animals, litters, cultures, etc.)
☐	☒ A description of how samples were collected, noting whether measurements were taken from distinct samples or whether the same sample was measured repeatedly
☐	☒ A statement indicating how many times each experiment was replicated
☐	☒ The statistical test(s) used and whether they are one- or two-sided (note: only common tests should be described solely by name; more complex techniques should be described in the Methods section)
☐	☒ A description of any assumptions or corrections, such as an adjustment for multiple comparisons
☐	☒ The test results (e.g. *P* values) given as exact values whenever possible and with confidence intervals noted
☐	☒ A clear description of statistics including central tendency (e.g. median, mean) and variation (e.g. standard deviation, interquartile range)
☐	☒ Clearly defined error bars

See the web collection on statistics for biologists for further resources and guidance.

Software

Policy information about availability of computer code

7. Software

Describe the software used to analyze the data in this study.

No custom code was used to analyze the data presented in this study.

Analysis of flow cytometry data was done using FlowJo (Treestar) software.

The 2-photon microscope used for imaging was controlled by the MicroManager software suit while imaging experiments were analyzed using the Imaris software suite (Bitplane).

R environment was used for pre-proccessing and plotting of datasets (previously published and novel datasets generated here).

Kaplan-Meier survival plots were generated using the Survival package in R

Wilcoxon rank-sum test statistics and p-values were calculated using the wilcox.exact function from the exactRankTests R package and q-values were

calculated using the q-value function in the Bioconductor R package.

A heatmap of population frequency out of total CD45+ or HLA-DR+ cells (as indicated) was made using the clustermap method from the seaborn python module.

Sequenced RNAseq library reads were then aligned against a reference of ribosomal RNA (rRNA) and mitochondrial RNA to deplete the dataset of rRNA and mtRNA using the Burrows-Wheeler Aligner. The remaining reads were then aligned to the Ensembl GrCh38.85 transcriptome build using the software package RSEM with the alignment tool Bowtie 2.

Statistical analyses and some plotting was performed using the software Prism (GraphPad).

Flow cytometry data were collected using FACSDiva (BD Bioscience).

For manuscripts utilizing custom algorithms or software that are central to the paper but not yet described in the published literature, software must be made available to editors and reviewers upon request. We strongly encourage code deposition in a community repository (e.g. GitHub). *Nature Methods* guidance for providing algorithms and software for publication provides further information on this topic.

Materials and reagents

Policy information about availability of materials

8. Materials availability

Indicate whether there are restrictions on availability of unique materials or if these materials are only available for distribution by a for-profit company.

All materials used in this study are either publicly available or will be made available for sharing with the research community upon publication of this study.

9. Antibodies

Describe the antibodies used and how they were validated for use in the system under study (i.e. assay and species).

Antibodies against human antigens:
CD45 clone HI30 (eBioscience 47-0459-42), CD3e clone OKT3 (eBioscience 46-0037-42), HLA-DR clone L243 (eBioscience 48-9952-42), CD56 clone CMSSB (eBioscience 46-0567-42), CD56 clone HCD65 (BioLegend 318304), CD19 clone H1B19 (eBioscience 46-0198-42 and 56-0199-42), CD14 clone 61D3 (Invitrogen Q10056; Cohort 1), CD14 clone M5E2 (BioLegend 301836; Cohort 2), CD16 clone 3G8 (BioLegend 302040), CD11c clone 3.9 (eBioscience 56-0116-42), CD85g clone 17G10.2 (eBioscience 12-5179-42), BDCA1 clone L161 (BioLegend 331516), BDCA3 clone AD5-14H12 (Miltenyi 130-090-513), CD4 clone RPA-T4 (BioLegend 300550), CD8 clone RPA-T8 (BioLegend 301040), CD25 clone BC96 (BioLegend 302612), CD25 clone 2A3 (eBioscience 17-0259-42), FoxP3 clone PCH101 (eBioscience 77-5776-40), FoxP3 clone 236A/E7 (eBioscience 25-4777-42), PD-1 clone EH-12 (BioLegend 329930), CTLA4 clone BNI3 (BioLegend 369606), TCR clone B1.1 (BioLegend 331212), Flt3L (Abcam ab9688).

Antibodies against mouse antigens:
CD3 clone 17A2 (BioLegend 100237 and 100244), CD4 clone RM4-5 (BioLegend 100545 and 100510), CD4 clone GK13 (BioLegend 100403), CD8 clone 53-6.7 (BioLegend 100734), CD11b clone M1/70 (BioLegend 101257), CD11c clone N418 (BioLegend 117339 and 117338), CD19 clone 6D5 (BioLegend 115522), CD24 clone M1/69 (BioLegend 101822), CD45 clone 30-F11 (BioLegend 103139, 103132, and 103114; eBioscience 56-0451-82), CD45R clone RA3-6B2 (BioLegend 103247, 103246, and 103226), CD69 clone H1.2F3 (eBioscience 25-0691-81), CD90.2 clone 30-H12 (BioLegend 105331), CD103 clone 2E7 (BioLegend 121406 and 121414), F4/80 clone BM8 (BioLegend 123108), Flt3L (R&D Systems AF427), Ly6C clone HK1.4 (BioLegend 128037), Ly6G clone 1A8 (BioLegend 127645), MHC-II clone M5/114.15.2 (BioLegend 707631), NK1.1 clone PK136 (BioLegend 108707, 108720, and 108749), Streptavidin-Brilliant Violet 650 (BioLegend 405231), Streptavidin-APC (eBioscience 17-4317-82).

Depleting and isotype control antibodies (mouse): CD8 clone 2.43 (BioXCell BE0061), CD4 clone GK1.5 (BioXCell BE0003-1), NK1.1 clone PK136 (BioXCell BE0036), and IgG2a isotype control (BioXCell BE0085).

All antibodies were titrated and tested for their ability to detect their ligand.

10. Eukaryotic cell lines

a. State the source of each eukaryotic cell line used.

All cell lines were purchased from ATCC.

b. Describe the method of cell line authentication used.

No cell lines were authenticated in these studies, but low passage number cell lines were utilized.

c. Report whether the cell lines were tested for mycoplasma contamination.

All eukaryotic cell lines used in this study tested negative by PCR for mycoplasma contamination.

d. If any of the cell lines used are listed in the database of commonly misidentified cell lines maintained by ICLAC, provide a scientific rationale for their use.

No commonly misidentified cells lines were used in this study.

Animals and human research participants

Policy information about studies involving animals; when reporting animal research, follow the ARRIVE guidelines

11. Description of research animals

Provide details on animals and/or animal-derived materials used in the study.

All mice were housed and bred at the University of California, San Francisco and maintained under specific pathogen-free conditions in accordance with the regulatory standards of the NIH and American Association of Laboratory Animal Care standards, and are consistent with the UCSF Institution of Animal Care and Use Committee (IACUC approval: AN170208-01B).

All animal experiments were undertaken in 6-8 week old animals. All experiments used age and sex matched animals.

Animal experiments in Figure 3a and Supplementary Figure 5a (Il2rg–/– vs WT) are female animals but showed similar results in replicates in male animals.

Animal experiments in Figure 3B and Supplementary Figure 5b-c (mixed bone marrow chimeras) were female animals.

Animal experiments in Figure 3C and Supplementary Figure 5D (Rag–/– vs. WT) were male animals.

Animal experiments in Figure 3D and Supplementary Figure 5e-f (NK-depletion experiment) were male animals with similar effects see in female animals in replicate experiments.

All imaging experiments used male animals (Figure 4).

C57Bl/6 (WT) mice were purchased from The Jackson laboratory or Simonsen Laboratories or bred in house. The Flt3l–/–, Il2rg–/– , and Ncr1-GFP mouse strains were purchased from The Jackson Laboratory. Ncr1-GFP mice were used as heterozygous animals as the knock-in disrupts gene expression.

The Flt3lreporter mice were generated, by contract, by the company Biocytogen. The P2AiCreERT2-T2A-TFP sequence was inserted between exon 8 and the 3'-UTR of Flt3l at the endogenous locus using CRISPR-Cas9 targeting. Proper insertion of the reporter construct was confirmed by PCR and DNA sequencing. Genotyping of Flt3l-reporter mice was done by PCR using a common forward primer that binds in the Flt3l locus: (5'-AAGGAGTCCCATAGCCCTAGAAGCC-3'), a WT reverse primer that binds in the Flt3l gene (5'-CTCCACAGCTTACGATTGTCGGAGC-3'), and a knock-in reverse primer specific to the iCreERT2 knock-in (5'-CCTGTCCCTGAACATGTCCATCAG-3'). Flt3l-reporter mice were crossed onto the PyMT-mCherry-OVA spontaneous tumor model background and offspring were screened for the PyMT-ChOVA transgene and the Flt3l-reporter knock-in by PCR. Female PyMT-ChOVA; Flt3l-reporter animals were monitored for tumors and used at 20 to 30 weeks of age.

To generate BM chimeras 6-8 week old Flt3l–/– mice were lethally irradiated by exposure to 1,100 rads of irradiation in 2 doses, 3 hours apart. 2-5 x106 BM cells, consisting of 50% Il2rg–/– and 50% WT or Flt3l–/– BM were injected retro-orbitally to reconstitute irradiated mice. Chimeric mice were injected with subcutaneous B16F10 tumor cells 8 weeks after reconstitution.

12. Description of human research participants

Describe the covariate-relevant population characteristics of the human research participants.

Patients were enrolled in this study if they had histologically confirmed stage IV or III unresectable metastatic melanoma. Patients were consented for tissue collection under a UCSF IRB approved protocol (UCSF CHR #13-12246). The study enrollment period started from December 2012 to November 2016, and the sample size was determined by the availability of specimens throughout this period. Patients were treated with the following anti-PD-1/PDL-1 axis blocking monoclonal antibodies: pembrolizumab (Keynote 001, 002, 006 or expanded access program or commercial supply) or nivolumab (commercial supply).

Melanoma cohort A patient selection and sample collection: Cutaneous/ subcutaneous metastatic melanomas (including metastases to the lymph node) were biopsied with either a punch (4 mm or 6 mm), a surgical excision, or core biopsies (16 g or 18 g) exclusively. Patients in cohort A (n = 33 patients with n = 35 samples) were selected without regard to prior treatment with immunotherapies, therefore in this cohort there is a range of patients from immunotherapy naïve to patients having been treated with anti-PD-1, ipilimumab, and/or IL-12 (Supplementary Table 2). Samples suspected to be the primary melanoma lesion are noted in Supplementary Table 2.

Melanoma cohort B patient selection and sample collection: Cutaneous/ subcutaneous tumors were biopsied with either a punch (4 mm or 6 mm), a surgical excision (sample K10), and all other tumor biopsies were with core biopsies (16 g or 18 g) exclusively. An additional sample was sent for pathology evaluation. Biopsies (n = 23) were collected prior to infusion of anti-PD-1 (Supplementary Table 2). All patients in cohort B received anti-PD-1 treatment after biopsy.

For both Cohort A and Cohort B patients were selected independent of age and sex. For both cohorts the only selection criteria was that the patient had stage III or IV metastatic melanoma and for cohort B that the patient was naive for anti-PD-1 treatment. The age range is 24-91 years of age for all patient samples with known age (cohort A and B combined). Cohort A had approximately 59.4% male and 40.6% female patients and Cohort B had approximately 61% male and 39% female patients. These values are estimates because age and sex is not available for every sample.

The fresh biopsy samples (cohort A and B) were immediately placed in a sterile container on saline soaked gauze (or submerged in PBS) and placed in a container of wet ice for transport to the laboratory for evaluation. Patient samples were coded and flow analysis and outcome data was scored by separate individuals prior to data agglomeration. All samples were processed and analyzed by flow cytometry, but only those with at least 1,000 live CD45+ cell events were included in the analysis.

All response evaluation was with radiologic imaging and limited to best overall response using the Response Evaluation Criteria in Solid Tumors version 1.1 (RECIST). Complete Response was defined as a complete regression of all target and non-target lesions, Partial Response was defined as regression of target lesions > 30 % with no new lesions appearing, Stable disease was defined as ≤ 30 % decrease or ≤ 20 % increase in the size of target lesions. Progressive disease was defined as increases in target lesions ≥ 20 % or appearance of new lesions > 1 cm in size. Patients with complete or partial response were classified as “responders” while those with stable disease or progressive disease were classified as “non-responders”.

nature research

Corresponding author(s): Matthew F. Krummel

☐ Initial submission ☐ Revised version ☒ Final submission

Flow Cytometry Reporting Summary

Form fields will expand as needed. Please do not leave fields blank.

Data presentation

For all flow cytometry data, confirm that:

☒ 1. The axis labels state the marker and fluorochrome used (e.g. CD4-FITC).

☒ 2. The axis scales are clearly visible. Include numbers along axes only for bottom left plot of group (a 'group' is an analysis of identical markers).

☒ 3. All plots are contour plots with outliers or pseudocolor plots.

☒ 4. A numerical value for number of cells or percentage (with statistics) is provided.

Methodological details

5. Describe the sample preparation.

Human Tissue Digestion: Cohort A tissue was vigorously minced with surgical scissors and transferred to a GenleMACs™ C Tube (Miltenyi Biotec) with 100 µg/mL Liberase TL (Roche) and 200 µg/mL DNase I (Roche) at 3mL per gram of tissue. C Tubes were incubated in the GentleMACS™ octo dissociator (Miltenyi Biotec) with heaters following the manufacturers dissociation protocol (Miltenyi Biotec Tumor Dissociation Kit). 10mL of sort buffer (PBS + 2% fetal calf Serum (FCS) + 2mM EDTA) was added to samples and filtered through a 100 µm filter, spun down, and red blood cells lysed with 175mM ammonium chloride. Cohort B tissue was vigorously minced with surgical scissors and transferred to a 50 mL conical with 20 µL/mL Liberase TL (at 5 mg/mL, Roche) and 50 U/ml DNase I (Roche) per 0.3 g of tissue for 30 minutes at 37° C with 5 % CO2 with constant agitation. Samples were then filtered through a 70 µm filter, spun down, and re-suspended for staining 24.

Mouse tissue digestion: Tumors were dissected from mice and total weight of removed tumor tissue was determined. Tumors were then minced using scalpels and digested with 500 U/mL Collagenase IV (Sigma), 100 U/mL Collagenase I (Worthington) and 200 µg/mL DNAse I (Roche) per 0.3 grams of tumor weight for 30 minutes in a 50 mL conical tube at 37° C with constant shaking. After 30 minutes, 7 mL of PBS + 2% FCS + 2 mM EDTA was added to tubes and tumors were passed through a 100 µm cell strainer to remove large pieces of tumor. Large pieces of tumor were dissociated by pushing the cells through the 70 µm cell strainer with the plunger of a 5 mL syringe. To digest lymph nodes (LNs), LNs were carefully dissected from mice and cleaned of fat. Inguinal LN were taken as tumor draining. LNs were pierced and torn with sharp forceps in 24-well plates and incubated for 15 min at 37° C in 1 ml of digestion buffer (100 U/ml collagenase I, 500 U/ml collagenase IV, and 200 µg/ml DNAse I in RPMI-1640). After the first 15 min of incubation, cells were pipetted up and down repeatedly, then returned for a second 15-min incubation at 37° C. After digestion, LNs were washed with PBS + 2% FCS +2 mM EDTA and filtered through a 100-µm cell strainer before staining for flow cytometry.

6. Identify the instrument used for data collection.

Flow cytometry was performed on a BD Fortessa or Aria Fusion flow cytometer.

7. Describe the software used to collect and analyze

Data was collected using the BD Diva software (BD Biosciences). Analysis of

the flow cytometry data.	flow cytometry data was done using FlowJo (Treestar) software.
8. Describe the abundance of the relevant cell populations within post-sort fractions.	n/a
9. Describe the gating strategy used.	All samples were gated for single cells by FSC-H/FSC-A and FSC-W/FSC-A. Once single cells were gated live cells were gated using the Zombie Aqua fixable viability dye (BioLegend, 423102) or Zombie NIR fixable viability dye (BioLegend 423106). Populations were defined as follows: Human Myeloid populations: BDCA3+ DCs (CD45+, CD3–, HLA-DR+, CD16–, CD85g–, CD11c+, CD14–, BDCA1–, BDCA3+), BDCA1+ DCs (CD45+, CD3–, HLA-DR+, CD16–, CD85g–, CD11c+, CD14–, BDCA3–, BDCA1+), CD14+ TAMs (CD45+, CD3–, HLA-DR+, CD16–, CD85g–, CD11c+, CD14+), CD14– TAMs (CD45+, CD3–, HLA-DR+, CD16–, CD85g–, CD11c+, CD14–, BDCA3–, BDCA1–), CD16+ monocytes (CD45+, CD3–, HLA-DR+, CD16+), eosinophils (CD45+, SSC-Ahi, CD16–), neutrophils (CD45+, SSC-Ahi, CD16+), pDCs (CD45+, CD3–, HLA-DR+, CD16–, CD11c–, CD85g+). Human Lymphoid populations: HLADR– CD4+ T cells (CD45+, CD3+, HLA-DR–, CD4+, CD8–), HLADR– CD8+ T cells (CD45+, CD3+, HLA-DR–, CD8+, CD4–), HLADR– CD4– CD8– T cells (CD45+, CD3+, HLA-DR–, CD4–, CD8–), HLADR– CD4+ CD8+ T cells (CD45+, CD3+, HLA-DR–, CD4+, CD8=), HLADR+ CD4+ T cells (CD45+, CD3+, HLA-DR+, CD4+, CD8–), HLADR+ CD8+ T cells (CD45+, CD3+, HLA-DR+, CD4–, CD8+), HLADR+ CD4+ CD8+ T cells (CD45+, CD3+, HLA-DR+, CD4+, CD8+), HLADR+ CD4– CD8– T cells (CD45+, CD3+, HLA-DR+, CD4–, CD8–), PD1+ CTLA4+ CD8+ T cells (CD45+, CD3+, HLA-DR–, CD4+, CD8–, PD1+, CTLA4+), PD1– CTLA4– CD8+ T cells (CD45+, CD3+, HLA-DR–, CD4–, CD8+, PD1–, CTLA4–), PD1+ CD8+ T cells (CD45+, CD3+, HLA-DR–, CD4–, CD8+, PD1+, CTLA4–), CTLA4+ CD8+ T cells (CD45+, CD3+, HLA-DR–, CD4–, CD8+, CD25–, FoxP3–, PD1–, CTLA4+), PD1+ CTLA4+ Thelper cells (CD45+, CD3+, HLA-DR–, CD4+, CD8–, FoxP3–, CD25–, PD1+, CTLA4+), PD1– CTLA4– Thelper cells (CD45+, CD3+, HLA-DR–, CD4+, CD8–, FoxP3–, CD25–, PD1–, CTLA4–), PD1+ Thelper cells (CD45+, CD3+, HLA-DR–, CD4+, CD8–, FoxP3–, CD25–, PD1+, CTLA4–), CTLA4+ Thelper cells (CD45+, CD3+, HLA-DR–, CD4+, CD8–, FoxP3–, CD25–, PD1–, CTLA4+), Tregulatory Cells (CD45+, CD3+, HLA-DR–, CD4+, CD8–, FoxP3+), T cells (CD45+, CD3+, HLA-DR–, TCR+), NK T cells (CD45+, CD3+, HLA-DR–, CD56+), NK cells (CD45+, CD3–, HLA-DR–, CD4–, CD8–, CD56+), B cells (CD45+, CD3–, HLA-DR+, CD19+). Mouse Lymphoid Populations: NK cells (Lineage 2[MHC-II, B220, CD11b, Ly6C]–, CD45+, CD3–, NK1.1+), CD4 T cells (Lineage 2–, CD45+, CD3+, CD90.2+, CD4+), CD8 T cells (Lineage 2–, CD45+, CD3+, CD90.2+, CD4+) and B cells (CD3–, CD90.2–, CD11b–, Ly6C–, MHC-II+, B220+). Mouse Myeloid Populations: CD103+ DCs: (Lineage1 [CD90.2, CD45R, Ly6G, NK1.1]–, CD45+, Ly6C–, MHC-II+, F4/80–, CD24+, CD103+), CD11b+ DCs: (Lineage1–, CD45+, Ly6C–, MHC-II+, F4/80–, CD24+, CD103–), Monocytes (CD45+, CD11b+, Ly6Chi), and neutrophils (CD45+, CD11b+,Ly6Cmid).

Tick this box to confirm that a figure exemplifying the gating strategy is provided in the Supplementary Information. ☒